NASA/TM–2009–215952

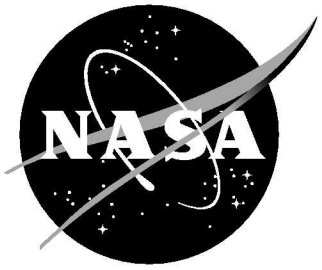

Exploring a Method for Improving Turbulent Separated-Flow Predictions with k-ω Models

C. L. Rumsey
Langley Research Center, Hampton, Virginia

December 2009

NASA STI Program ... in Profile

Since its founding, NASA has been dedicated to the advancement of aeronautics and space science. The NASA scientific and technical information (STI) program plays a key part in helping NASA maintain this important role.

The NASA STI Program operates under the auspices of the Agency Chief Information Officer. It collects, organizes, provides for archiving, and disseminates NASA's STI. The NASA STI Program provides access to the NASA Aeronautics and Space Database and its public interface, the NASA Technical Report Server, thus providing one of the largest collection of aeronautical and space science STI in the world. Results are published in both non-NASA channels and by NASA in the NASA STI Report Series, which includes the following report types:

- TECHNICAL PUBLICATION. Reports of completed research or a major significant phase of research that present the results of NASA programs and include extensive data or theoretical analysis. Includes compilations of significant scientific and technical data and information deemed to be of continuing reference value. NASA counterpart of peer-reviewed formal professional papers, but having less stringent limitations on manuscript length and extent of graphic presentations.
- TECHNICAL MEMORANDUM. Scientific and technical findings that are preliminary or of specialized interest, e.g., quick release reports, working papers, and bibliographies that contain minimal annotation. Does not contain extensive analysis.
- CONTRACTOR REPORT. Scientific and technical findings by NASA-sponsored contractors and grantees.
- CONFERENCE PUBLICATION. Collected papers from scientific and technical conferences, symposia, seminars, or other meetings sponsored or co-sponsored by NASA.
- SPECIAL PUBLICATION. Scientific, technical, or historical information from NASA programs, projects, and missions, often concerned with subjects having substantial public interest.
- TECHNICAL TRANSLATION. English- language translations of foreign scientific and technical material pertinent to NASA's mission.

Specialized services also include creating custom thesauri, building customized databases, and organizing and publishing research results.

For more information about the NASA STI Program, see the following:

- Access the NASA STI program home page at ***http://www.sti.nasa.gov***
- E-mail your question via the Internet to help@sti.nasa.gov
- Fax your question to the NASA STI Help Desk at 443-757-5803
- Phone the NASA STI Help Desk at 443-757-5802
- Write to:
  NASA STI Help Desk
  NASA Center for AeroSpace Information
  7115 Standard Drive
  Hanover, MD 21076–1320

NASA/TM–2009–215952

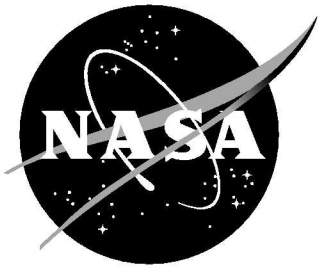

Exploring a Method for Improving Turbulent Separated-Flow Predictions with k-ω Models

C. L. Rumsey
Langley Research Center, Hampton, Virginia

National Aeronautics and
Space Administration

Langley Research Center
Hampton, Virginia 23681-2199

December 2009

Available from:

NASA Center for AeroSpace Information
7115 Standard Drive
Hanover, MD 21076-1320
443-757-5802

Abstract

A particular failing of Reynolds-averaged Navier-Stokes separated turbulent flow computations is addressed within the context of a k-ω two-equation turbulence model. The failing is the tendency for turbulence models to under-predict turbulent shear stress in the shear layers of some separation bubbles, yielding late boundary layer reattachment and recovery. Inspired by unpublished work of Volker, Langtry, and Menter, the author undertook an independent investigation in an attempt to improve the ability of the Menter shear stress transport (SST) model to predict flowfield characteristics in and downstream of separation bubbles. The fix is an ad hoc term that is a function of the local ratio of turbulent production to dissipation; it is used to multiply the ω-destruction term, increasing eddy viscosity in separated regions. With this fix, several flowfields are investigated. Results show that, although the "separation fix" can provide dramatic improvement in some cases, it is not consistently good for all flows. Thus, although it may prove helpful in many situations in its current form, this model may benefit from further refinements, including better sensitization to the energetics of turbulence in the separated region.

1 Introduction

It is well-established that Reynolds-averaged Navier-Stokes (RANS) turbulence models often do a poor job representing separation bubble physics, especially downstream reattachment and recovery. A very-well documented case is the 2-D hump model (see, e.g., Rumsey [1]). Another well-known case is flow over a hill [2]. Although many modern models can adequately predict the onset of smooth-body separation, in the shear layer region of separated bubbles the eddy viscosity can be under-predicted. This under-prediction results in too little mixing in the separated region, and consequently a delay in reattachment and flow recovery.

It has also been noted that some models (notably k-ε variants) are often unable to predict the onset of smooth-body separation correctly (e.g., Wilcox [3], Rumsey [2]). By predicting the onset of separation too late, these models tend to predict shorter bubble size. Sometimes, the shorter bubbles coincidentally agree better with experiment, but this is for the wrong reasons. Turbulent shear stress levels within the bubble are still often under-predicted by k-ε models; the only reason why the bubble is shorter is because of its (incorrect) delayed separation.

As discussed in Rumsey [1], large eddy simulation (LES) methods, as well as some hybrid RANS-LES methods, have demonstrated dramatic improvement compared to RANS for separated flows. This improvement is due to the fact that in the separation bubble, the large eddies are resolved in space and time. By capturing the turbulent eddy motion, the separated flow physics are better represented. Of course, this improvement comes at a great cost, because LES and RANS-LES computations are necessarily 3-D and time-accurate on

highly resolved grids.

It seems reasonable to assume that RANS models could be improved to better approximate separated flow physics. After all, in attached turbulent boundary layers, RANS (with an eddy viscosity model) is doing no more than approximating the *average* effects of random turbulent eddies through the action of a mean local eddy viscosity. Currently, turbulence models are under-estimating the average effects of the larger (and more energetic) eddies that are present in reality in separated bubble shear layers. Perhaps it is reasonable to attempt to improve this modeling through increased eddy viscosity inside the bubble. This idea was briefly explored in a simple numerical test in Rumsey [4] and was found to be viable. If successful, improved RANS modeling would offer a far less expensive alternative to LES and RANS-LES time-dependent simulations, particularly for nominally two-dimensional configurations.

The current paper explores an idea suggested to the author.[1] It is based on unpublished work by Volker, Langtry, and Menter. However, other than the idea to make use of the ratio of local turbulence production over dissipation to trigger an increase in eddy viscosity, the fix and its implementation are original. The unpublished method of Volker, Langtry, and Menter is proprietary (it is implemented in a commercial CFD code), and its details are unknown to the author. The current method described in this paper should be thought of as a complementary exploration of a possible technique to improve the predictive behavior of k-ω models for separated flows. Further improvements are certainly possible. Using steady-state RANS, the two-equation Menter shear stress transport (SST) model is employed as the vehicle for testing the technique, although the fix should be equally applicable to any k-ω model.

The paper is organized as follows. First, the standard SST model is described, followed by details concerning the separation fix. A brief overview of the CFD code's numerics is then given. For results, the following separated cases are computed: hill, backstep, diffuser, hump (without and with flow control), and axisymmetric bump. Finally, conclusions are drawn.

2 The Two-Equation Turbulence Model

2.1 Menter k-ω SST Model

The two-equation SST model of Menter [5] can be written as:

$$\frac{Dk}{Dt} = \frac{\mathcal{P}}{\rho} - \beta^* \omega k + \frac{\partial}{\partial x_j}\left[(\nu + \sigma_k \nu_t)\frac{\partial k}{\partial x_j}\right] \tag{1}$$

$$\frac{D\omega}{Dt} = \frac{\gamma}{\mu_t}\mathcal{P} - F_{sf}\beta\omega^2 + \frac{\partial}{\partial x_j}\left[(\nu + \sigma_\omega \nu_t)\frac{\partial \omega}{\partial x_j}\right] + 2(1-F_1)\frac{\sigma_{\omega 2}}{\omega}\frac{\partial k}{\partial x_j}\frac{\partial \omega}{\partial x_j} \tag{2}$$

where in the standard SST model the new separation fix parameter $F_{sf} \equiv 1$. Details concerning F_{sf} will be given below. The eddy viscosity is given by:

[1] Menter, F., private communication, 2009.

$$\mu_t = \rho \frac{a_1 k}{\max(a_1 \omega, \Omega F_2)} \tag{3}$$

where $a_1 = 0.31$, Ω is the magnitude of vorticity, and F_1 and F_2 are blending functions (given below). Furthermore, $\nu = \mu/\rho$ and $\nu_t = \mu_t/\rho$.

The production term $\mathcal{P}$ is given by

$$\mathcal{P} = -\tau_{ij} \frac{\partial u_i}{\partial x_j} \tag{4}$$

where

$$\tau_{ij} = \rho \overline{u_i u_j} = -2\mu_t \left(S_{ij} - \frac{1}{3} \frac{\partial u_k}{\partial x_k} \delta_{ij} \right) + \frac{2}{3} \rho k \delta_{ij} \tag{5}$$

$$S_{ij} = \frac{1}{2} \left(\frac{\partial u_i}{\partial x_j} + \frac{\partial u_j}{\partial x_i} \right) \tag{6}$$

Note that the definition for τ_{ij} varies in the literature: sometimes it is defined with the opposite sign, and sometimes it is defined without the density. The definition does not matter as long as the production term is defined appropriately in Eq. (4), with $+2\mu_t S_{ij}(\partial u_i/\partial x_j)$ as the leading term in $\mathcal{P}$. In Eq. (5), the $-(1/3)(\partial u_k/\partial x_k)\delta_{ij}$ term and the $(2/3)\rho k \delta_{ij}$ term are often ignored for low-speed flows (the former term makes the strain rate tensor traceless in 3-D flows).

In an often-used variant of the k-ω model, the production term is simplified by an approximation that makes use of the local magnitude of vorticity Ω:

$$\mathcal{P} = \mu_t \Omega^2 - \frac{2}{3} \rho k \delta_{ij} \frac{\partial u_i}{\partial x_j} \tag{7}$$

This vorticity source term is often a good approximation of the exact source term in boundary layer flows [6], and its use can avoid some numerical difficulties associated with the use of the exact source term. It is used for all results in this paper. Again, it is often common to ignore the $(2/3)\rho k \delta_{ij}$ term in the production source of Eq. (7) for many low-speed applications.

The "shear stress transport" (SST) part of the model is based on Bradshaw's hypothesis [7] that the principal shear stress is proportional to k, via: $\tau_{12} = -\rho a_1 k$. From Eq. (5), the primary term in eddy viscosity models is: $\tau_{12} = -2\mu_t S_{12}$. In adverse pressure gradient boundary layer flows, the standard method often leads to too much eddy viscosity (an over-prediction of τ_{12}), inhibiting or delaying separation. In these situations, it is better for the model to choose τ_{12} based on Bradshaw's hypothesis. Using:

$$\rho a_1 k = 2\mu_t S_{12} \tag{8}$$

we find how to set the eddy viscosity in order to recover values corresponding with Bradshaw's hypothesis:

$$\mu_t = \frac{\rho a_1 k}{2S_{12}} \approx \frac{\rho a_1 k}{\Omega} \tag{9}$$

Functionally, Eq. (3) chooses the minimum eddy viscosity between the standard one and that dictated by Bradshaw's hypothesis limited to within the boundary layer region.

In the SST model, there are two sets of coefficients that are combined using a blending function. The constants for set 1 are $\beta_1^* = 0.09$, $\sigma_{k1} = 0.85$, $\beta_1 = 0.075$, $\sigma_{\omega 1} = 0.5$, and $\gamma_1 = \beta_1/\beta_1^* - \sigma_{\omega 1}\kappa^2/\sqrt{\beta_1^*} \approx 0.55317$. The constants for set 2 are $\beta_2^* = 0.09$, $\sigma_{k2} = 1.0$, $\beta_2 = 0.0828$, $\sigma_{\omega 2} = 0.856$, and $\gamma_2 = \beta_2/\beta_2^* - \sigma_{\omega 2}\kappa^2/\sqrt{\beta_2^*} \approx 0.44035$. The constant κ is defined as $\kappa = 0.41$. Set 1 and set 2 are blended via:

$$\phi = F_1\phi_1 + (1 - F_1)\phi_2 \tag{10}$$

and

$$F_1 = \tanh(arg_1^4) \tag{11}$$

$$arg_1 = \min\left[\max\left(\frac{\sqrt{k}}{0.09\omega d}; \frac{500\nu}{d^2\omega}\right); \frac{4\rho\sigma_{\omega 2}k}{CD_{k\omega}d^2}\right] \tag{12}$$

$$CD_{k\omega} = \max\left(2\rho\sigma_{\omega 2}\frac{1}{\omega}\frac{\partial k}{\partial x_j}\frac{\partial \omega}{\partial x_j}; 10^{-20}\right) \tag{13}$$

where d is the distance to the nearest wall. The F_2 term is given by:

$$F_2 = \tanh(arg_2^2) \tag{14}$$

$$arg_2 = \max\left(2\frac{\sqrt{k}}{0.09\omega d}; \frac{500\nu}{d^2\omega}\right) \tag{15}$$

2.2 Description of the Separation Fix

The new separation fix parameter is defined as follows:

$$F_{sf} = f_d\left\{\min\left(12, \max\left[1, \left(4\frac{\mathcal{P}}{\varepsilon} - 5\right)\right]\right)\right\} + (1 - f_d) \tag{16}$$

where

$$f_d = 1 - \tanh\left([8r_d]^3\right) \tag{17}$$

$$r_d = \frac{\mu_t + \mu}{\rho\kappa^2 d^2\sqrt{\frac{\partial u_i}{\partial x_j}\frac{\partial u_i}{\partial x_j}}} \tag{18}$$

Within the context of the current k-ω model, the production-to-dissipation ratio is obtained via:

$$\frac{\mathcal{P}}{\varepsilon} = \frac{\mu_t \Omega^2}{0.09 \rho k \omega} \tag{19}$$

The rationale for the form of Eq. (16) is the following. Volker, Langtry, and Menter noted in their unpublished work that in separated shear layer regions where turbulent shear stress is under-predicted, the $\mathcal{P}/\varepsilon$ tends to be significantly larger than 1, and often as high as $3-4$. In most boundary layers, wakes, jets, etc., $\mathcal{P}/\varepsilon < 1.5$ or so. In the current work, a function was devised that remains 1 when $\mathcal{P}/\varepsilon < 1.5$, and quickly increases (to a maximum of 12 when $\mathcal{P}/\varepsilon \geq 4.25$) for larger values. (This maximum of 12 was chosen merely to keep F_{sf} bounded. The fix is not believed to be particularly sensitive to this number, so long as it is not too small.) In order to minimize the impact of the function on the SST model's previously-calibrated ability to compute attached boundary layers and separation points, the function is turned off inside boundary layers through the use of the f_d function from Spalart et al. [8]. This function is intended to be 1 in LES regions and 0 elsewhere. The SST's F_1 blending function – used as $(1 - F_1)$ in place of f_d in Eq. (16) – was also attempted in the beginning of this study, but it tended to be much less smoothly behaved (and hence numerically more problematic) than f_d in the separated shear layer region.

The model represented by Eq. (16) is not derived from rigorous physics, but rather represents an ad hoc fix based on the recognition that a specific local turbulent quantity ($\mathcal{P}/\varepsilon$) could be used to identify an area where larger eddy viscosity levels may be warranted. The choice of influencing the eddy viscosity by increasing the ω destruction term was made based on success with similar implementation of a curvature correction fix [9, 10]. Other choices, such as increasing the k production term (done by Volker, Langtry, and Menter in their unpublished work) or increasing the eddy viscosity (Eq. (3)) directly were not attempted here. It should be noted that, because this model reduces ω in the separated shear region, both F_1 and F_2 (Eqs. (11) and (14)) are typically affected when $\mathcal{P}/\varepsilon > 1.5$, somewhat extending the area in which these blending functions equal 1 in the separated shear region.

3 Numerical Method

The computer code CFL3D [11] solves the three-dimensional, time-dependent, Reynolds averaged compressible Navier-Stokes equations with an upwind finite-volume formulation (it can also be exercised in two-dimensional mode of operation for 2-D cases). It can solve flows over multiple-zone grids that are connected in a one-to-one, patched, or overset manner, and can employ grid sequencing, multigrid, and local time stepping when accelerating convergence to steady state. Second-order accurate upwind-biased spatial differencing is used for the inviscid terms, and flux limiting is used to obtain smooth solutions in the vicinity of shock waves, when present. Viscous terms are centrally differenced with second-order accuracy. For very low Mach number flows, precondition-

ing [12] is used to insure convergence and accuracy of the solutions. The code can use either full Navier-Stokes (including all cross-derivative viscous terms) or thin-layer (for which cross-derivative viscous terms are neglected and viscous derivatives in specific coordinate directions can be ignored). For all results in this paper, full Navier-Stokes was employed.

The CFL3D code is advanced in time with an implicit approximate factorization method. The implicit derivatives are discretized as spatially first-order accurate, which results in block tridiagonal inversions for each sweep. However, for solutions that utilize Roe flux-difference splitting [13], the block tridiagonal inversions are further simplified using a diagonal algorithm with a spectral radius scaling of the viscous terms.

The turbulence models are solved uncoupled from the mean flow equations using implicit approximate factorization. Their advective terms are discretized using first-order accurate upwind differencing. In all cases presented in this paper, turbulence models were integrated all the way to the wall (no wall functions), and minimum y^+ levels in all grids were less than 1, even on the coarser grids.

For boundary conditions, the two-equation k-ω turbulence model used the following. At solid walls, $k_w = 0$ and $\omega_w = 60\mu_w/(\rho_w \beta_1 d_1^2)$, where d_1 is the distance to the first cell center off the wall. In the freestream, $k_\infty/(a_{ref}^2) = 9 \times 10^{-9}$ and $\omega_\infty \mu_{ref}/(\rho_{ref} a_{ref}^2) = 1 \times 10^{-6}$, giving $\mu_{t,\infty}/\mu_{ref} = 0.009$.

4 Results

4.1 2-D Hill

The 2-D hill case was originally an experiment reported by Almeida et al. [14]. Jang et al. [15] modified the geometry and test conditions for their LES study, which subsequently served as a reference for a RANS workshop [16]. The Jang et al.LES results also serve as a reference for evaluating the RANS results here. The Mach number for the 2-D hill case was very low (M=0.001), so preconditioning was employed in CFL3D. The Reynolds number was 10,595 per hill height H. At the upstream boundary, the velocity and turbulence levels were specified based on the LES data, and the pressure was extrapolated from the interior of the grid. At the downstream boundary the pressure was set to $p/p_{ref} = 1$, and all other quantities were extrapolated from the interior of the grid. Both bottom and top walls were no-slip adiabatic. Fig. 1 shows a picture of the grid, with every fourth gridpoint shown in both coordinate directions for clarity.

Results showing separation and reattachment location on the fine (737×193), medium (369×97), and coarse (185×49) grids using SST and SST including the "separation fix," termed SST-sf, are shown in Fig. 2. As with all grid studies to be shown in this paper, the medium grid was made from every other point in each coordinate direction of the fine grid, and the coarse grid was every other point from the medium grid. Locations are plotted as a function of

$\sqrt{1/N}$, where N is the number of grid cells. For 2-D, $\sqrt{1/N}$ is proportional to the average grid spacing, Δh. Here, Δh is used rather than Δh^2 because the results of interest (separation and reattachment locations) converge in this case with close to first order accuracy, likely because of the use of first-order wall boundary conditions in CFL3D. The finer the grid, the closer $\sqrt{1/N}$ approaches zero (infinite refinement). As described in Rumsey [2], many models that predict the separation location reasonably well (say, within $15 - 20\%$), including SST, predict too long a separation bubble compared to the LES reference (which agrees well with experiment). This is because the turbulence mixing is under-predicted inside the bubble. Here, SST-sf significantly improved the SST results compared to LES. Standard SST over-predicted the reattachment location by 63% on the fine grid, whereas SST-sf over-predicted by only 13%.

Contours of $\mathcal{P}/\varepsilon$, using Eq. (19) and the SST-sf model, are shown in Fig. 3. This figure illustrates how this particular quantity had levels significantly greater than 1.5 in the separated shear region. Fig. 4 shows the resulting contours of F_{sf} for the SST-sf solutions. The contours were identically 1 most places in the flowfield, and only exceeded 1 in the separated shear region. The increase in the eddy viscosity for the SST-sf model compared to SST in the separated region can be seen in Fig. 5. Note that the eddy viscosity is affected throughout the separated region, and not just in the thin layer where $\mathcal{P}/\varepsilon$ is high. Streamlines are shown in Fig. 6.

Profiles of velocity, nondimensionalized by upstream reference velocity U_{ref}, are plotted at ten stations in Fig. 7. Both models performed well in the initial separation region, through $x/H = 3$, but beyond that the SST-sf model reattached and recovered quicker. Profiles of turbulent shear stress ($\overline{u'v'}$) and turbulent kinetic energy (k), both nondimensionalized by U_{ref}^2, are plotted in Figs. 8 and 9, respectively. In these figures it is clearly seen that SST under-predicted $\overline{u'v'}$ and k peak magnitudes throughout the separated region. The SST-sf model agreed better with the LES results, although its peak levels were still severely under-predicted at $x/H = 0.5$ and 1.0. This under-prediction is at least in part due to the fact that the fix is switched off in near-wall regions via the f_d function to avoid affecting the already well-calibrated SST model inside boundary layers.

4.2 2-D Backstep

The 2-D backstep is a separated case for which the standard SST model already does a reasonably good job compared to experiments [5]. (The one-equation Spalart-Allmaras (SA) model [17] also does fairly well; see Rumsey and Thomas [18].) This agreement brings up two questions. First, why do RANS models like SST and SA perform reasonably well in terms of predicting reattachment location for this separated case, but not for others like the hill and hump? (As will be seen below, standard SST does *not* dramatically under-predict the magnitude of the peak turbulent shear stress for this backstep case.) Second, given that SST already gives fairly good predictions, will the SST-sf

model make them worse?

Experimental data for the backstep case are from Driver and Seegmiller [19]. This is a "classic" case, often used to test turbulence models. A step of height H is in a tunnel with height $8H$ ($9H$ after the step). The Mach number is 0.128 and Reynolds number based on step height is 37,573. In the original experiment, the top wall was set to different angles, but here only the straight wall case was computed.

Fig. 10 shows the grid used, which consisted of three zones (97×257, 385×257, and 129×257), connected with a patched interface at the step and one-to-one downstream. Both bottom and top walls were no-slip adiabatic. At the outflow boundary, $p/p_{ref} = 1.00149$ and all other quantities were extrapolated from the interior. At the upstream boundary, the u-velocity profile was set to approximately match the reference boundary layer thickness and wall skin friction level. The k and ε values were specified in a way similar to that used by Monson et al. [20], as follows. In the near wall region ($y^+ < 4$), the values for k were obtained from the expression $k^+ = 0.05(y^+)^2$. The peak k was specified as $0.004U_{ref}^2$, and was assumed to be at $y^+ = 25$. The value of ε was computed from $\varepsilon = C_\mu^{3/4}K^{3/2}/L_m$, with $L_m = \kappa y$ in the inner region and $L_m = 0.09\delta$ in the outer region. Then, ω was obtained from $\omega = \varepsilon/k$. Also at the upstream boundary, the density was specified at $\rho/\rho_{\text{ref}} = 1$, and the pressure was extrapolated from the interior of the grid.

Fig. 11 shows the grid refinement effect on reattachment locations for the backstep using both SST and SST-sf, compared to experiment. The fine grid had 155,648 total cells, medium had 38,912, and coarse had 9728. In this case, SST slightly over-predicted the reattachment location by about 2% on the fine grid, but SST-sf under-predicted it by almost 35%. Contours of $\mathcal{P}/\varepsilon$ and F_{sf} for the SST-sf solutions are shown for three different grid levels in Figs. 12 and 13, respectively. The $\mathcal{P}/\varepsilon$ levels in the shear layer were greater than 4, consequently yielding F_{sf} values well in excess of 1. Streamlines are shown in Fig. 14, and bottom wall skin friction coefficient is shown in Fig. 15.

Fig. 16 shows u-velocity profiles and Fig. 17 shows turbulent shear stress profiles at three locations downstream of the step. At $x/H = 1$ and 4, the SST model matched experimental velocity very well, but did not recover quickly enough at $x/H = 6$. SST-sf results were poor at the first two stations, but better downstream. However, this was no doubt because it reattached too early. The SST model also predicted peak $\overline{u'v'}$ reasonably well, whereas SST-sf predicted too large a peak magnitude.

This test case suggests that, although SST-sf can improve the separated flow predictions for a particular case (e.g., the 2-D hill), the fix is not universal. For the backstep, although the SST-sf model performed as it was intended (augmenting the eddy viscosity in the separated shear region) the original SST model performed much better than SST-sf compared to experiment. In this case the peak nondimensional $\overline{u'v'}$ magnitudes from experiment were less than half those in the 2-D hill case. Perhaps enhancement of turbulent mixing in the shear layers of separation bubbles is not universally needed for RANS models,

and there may be some physics in the flowfield that dictate whether or not enhancement is called for. Certainly, the current results suggest that $\mathcal{P}/\varepsilon$ may not necessarily be the most appropriate indicator for it.

4.3 2-D Diffuser

The 2-D diffuser case is a one-sided diffuser that comes at the end of a fully-developed channel flow. The wall angle is 10°, and separation occurs on the sloped wall and then reattaches downstream. This experiment was performed by Obi et al. [21] and again later by Buice and Eaton [22]. Like the 2-D backstep, this is a configuration for which the standard SST model already does a reasonably good job, with the exception that separation is predicted somewhat early (see, e.g., Hirsch and Tartinville [23]). Some other modern RANS models also perform reasonably well. LES has also been very successful (see, e.g., Kaltenback et al. [24]).

The grid used was 865×193, shown (with every fourth point removed for clarity) in Fig. 18. The grid extended upstream to $x = -80$ and downstream to $x = 100$. The ramp itself ran from $x = 0$ to 20. The upstream channel height was $y = 1$ and downstream channel height was $y = 4.7$. There was wall curvature with radius $R = 9.7$ at the start and end of the ramp, as described in Buice and Eaton [22]. Reynolds number based on the upstream channel height was 20,000. The computations were performed using a reference Mach number of 0.2. At the inflow, total pressure and total temperature were set to $p_T/p_{ref} = 1.02828$ and $T_T/T_{ref} = 1.008$, respectively. At the outflow, $p/p_{ref} = 1.0$ and all other quantities were extrapolated from the interior. Top and bottom walls were adiabatic no-slip.

In this case, results using SST and SST-sf were essentially identical on all grid levels. This was because the $\mathcal{P}/\varepsilon$ in the separated shear layer was less than 1.5, so the F_{sf} parameter never became active (i.e., $F_{sf} = 1$ everywhere). A plot of $\mathcal{P}/\varepsilon$ is shown in Fig. 19. Streamlines on the finest grid are shown in Fig. 20. Separation occurred on the ramp near $x = 2.5$, then reattached downstream near $x = 29.2$. The bottom wall skin friction coefficient is shown in Fig. 21 on the three different grid densities, compared to the experiment of Buice and Eaton [22]. It can be seen that the SST and SST-sf results separated early compared to experiment, but reattached at approximately the correct location. Reattachment locations differed by only about 1% on the medium grid compared to the fine grid.

Profiles of u-velocity are shown at six different stations in Fig. 22, compared to experiment. Here, velocities are nondimensionalized by upstream bulk velocity U_{bulk}, the average velocity in the upstream channel [22]. Generally, comparison was very good in and near the separated and reattachment region. However, downstream recovery was too slow, as indicated at $x = 33.87$. Although not shown, this slow recovery persisted downstream, as also noted in Hirsch and Tartinville [23]. Turbulent shear stress profiles are shown in Fig. 23. If anything, the SST and SST-sf over-predicted the peak levels in magnitude. Overall, however, results were in reasonable agreement with the experiment.

4.4 2-D Hump without and with Flow Control

The 2-D hump case, originally tested by Seifert and Pack [25], was subsequently retested by Greenblatt et al. [26, 27] for the CFDVAL2004 validation workshop [28]. This test has served as a reference case for dozens of CFD studies. It is particularly useful because the case clearly demonstrates the underprediction of eddy viscosity by RANS turbulence models in the separated shear layer region at the back end of the hump, leading to too little mixing and hence too late a reattachment downstream. Methods like LES that resolve the unsteady 3-D turbulent eddies in the separated region have been shown to do a much better job [1].

The Mach number was 0.1 and Reynolds number was 936,000. Two conditions are shown here: no flow control and steady suction. Boundary conditions were set as follows. At the floor and hump surfaces, as well as at the side walls inside the cavity, solid wall adiabatic boundary conditions were applied. At the front of the grid, which extended to $x/c = -6.39$, far-field Riemann-type boundary conditions were applied. This boundary condition is essentially a non-reflective freestream condition; the location $x/c = -6.39$ was chosen so that the naturally-developing fully-turbulent boundary layer in the computation reached the same thickness as the experimentally measured value of approximately $\delta/c = 0.073$ at the location $x/c = -2.14$. At the downstream boundary (at $x/c = 4.0$) the pressure was set at $p/p_{\text{ref}} = 0.99962$, and all other quantities were extrapolated from the interior of the domain. This back pressure was chosen to achieve approximately the correct inflow conditions for steady flow. The top tunnel wall was treated as an inviscid wall. Its shape was contoured to approximately account for the effects of side plate blockage [4]. At the bottom of the cavity, for no-flow-control an Euler (slip) boundary condition was applied, and for steady suction a constant v-velocity $\rho v = -0.001248\rho_{ref}a_{ref}$ was used, with density and pressure extrapolated from the interior of the domain. This latter boundary condition was chosen to achieve a suction rate equivalent to approximately 0.01518 kg/s through a 23-inch-span slot.

Fig. 24 shows a picture of part of the grid, with every other gridpoint shown in both coordinate directions. The fine grid had 208,320 grid cells with 4 zones connected in a one-to-one fashion. Medium and coarse levels were created by taking every other point in each coordinate direction.

Computed separation and reattachment locations for no flow control on three different grid levels are shown in Fig. 25, as a function of $\sqrt{1/N}$. SST and SST-sf produced similar separation locations, but dramatically different reattachment locations. In this case, SST reattached too far downstream (11% in error from experiment on the finest grid), and SST-sf reattached too far upstream (5% in error on the finest grid). Streamlines are compared in Fig. 26, and confirm that the SST bubble was too big, while the SST-sf bubble was too small. For reference, the $\mathcal{P}/\varepsilon$ contours on the fine, medium, and coarse grids are shown in Fig. 27; corresponding F_{sf} contours from the SST-sf solutions are shown in Fig. 28.

Surface pressure coefficient and skin friction coefficient are displayed in

Fig. 29 for no flow control. Three grids are plotted for SST-sf, but only the finest grid result is shown for SST, for clarity of comparison. Profiles of nondimensional u-velocity and $\overline{u'v'}$ at four different span stations in and downstream of the separation bubble are plotted in Figs. 30 and 31, respectively. Again, only the fine grid SST result is displayed for clarity. Within the bubble itself, both SST and SST-sf produced similar velocity profiles, but SST-sf showed faster recovery and better agreement with velocity profiles downstream, at $x/c = 1.1$ and 1.3. SST-sf behaved as it was designed to, producing higher turbulent shear stress levels than SST downstream of separation, in better agreement with experimental levels.

Computed separation and reattachment locations for steady suction flow control are shown in Fig. 32. In this case, SST reattached 19% too far downstream on the fine grid, while SST-sf reattached in good agreement with experiment, only 4% too far downstream. Streamlines are shown in Fig. 33. Results using SST-sf were significantly better in comparison with experiment than SST. For reference, the $\mathcal{P}/\varepsilon$ contours on the fine, medium, and coarse grids are shown in Fig. 34, and corresponding F_{sf} contours from the SST-sf solutions are shown in Fig. 35.

Fig. 36 shows surface pressure coefficient and skin friction coefficient for the suction case (note that c_f was not measured in the experiment). Profiles of nondimensional u-velocity and $\overline{u'v'}$ are given in Figs. 37 and 38, respectively. Results for SST-sf were generally much better than results for SST, although the SST-sf turbulent shear stress levels at $x/c = 0.8$ and 0.9 were still dramatically too low in magnitude compared to the experiment. This disagreement indicates that the current ad hoc fix in the SST equations is not adequately reflecting the physics. Apparently, the suction in the experiment induces much more turbulent mixing within the bubble compared to no flow control (peak experimental $\overline{u'v'}$ magnitude at $x/c = 0.8$ is 0.04 in Fig. 38 compared to 0.02 in Fig. 31). But the models generated similar turbulence levels in both cases.

4.5 3-D Axisymmetric Bump

The 3-D axisymmetric bump case is a widely-used test case for shock-induced separated flow, followed by reattachment / recovery. The experiment was performed by Bachalo and Johnson [29]. Current 3-D results were computed on a fine $2 \times 721 \times 321$ grid, along with a medium and coarser level that used every other point in the latter two coordinate directions, successively. The two axisymmetric planes were separated by an angle of one degree. A picture of a portion of the grid is given in Fig. 39. The Mach number was 0.875, and Reynolds number was 2.66 million based on bump chordlength. The grid extended from about 3.2 chordlengths upstream to about 4.4 chordlengths downstream. The grid farfield extent was about 4 chordlengths above the bump. Boundary conditions were periodic (rotated through one degree) on the two axisymmetric planes, farfield Riemann-type upstream, downstream, and in the farfield, and no-slip adiabatic on the body.

Traditionally, this axisymmetric bump case is one for which the standard

SST model has been considered to perform reasonably well, although reattachment is slightly late and downstream recovery is somewhat too slow. However, the shock location, surface pressure coefficient, and bubble profiles are considered excellent [5].

When using SST-sf, results were essentially identical to the SST model. Plots of $\mathcal{P}/\varepsilon$ in Fig. 40 show that, other than at the shock, levels did not greatly exceed 1.5 in the separated shear layer on the fine grid. As a result, the F_{sf} levels, shown in Fig. 41, were very close to one (except at the shock). Even on the medium and coarse grids, for which $\mathcal{P}/\varepsilon$ levels were somewhat higher in the shear layer, the F_{sf} exceeded one only in a small area, and the levels were not very high. Streamlines are shown in Fig. 42 for the SST model on the fine grid. Results for SST-sf were identical.

Surface pressure coefficient and skin friction coefficient are shown in Fig. 43(a) and (b). Computed results were excellent compared with surface c_p. Profiles of velocity and turbulent shear stress are given in Figs. 44 and 45, respectively. Grid convergence was demonstrated in these figures, as well as fairly good agreement between CFD and experiment. The too-slow recovery downstream of reattachment (mentioned above) can be seen in the velocity plots downstream of $x/c = 1.125$. SST and SST-sf results for the fine grid were essentially identical.

5 Conclusions

This study was an exploration of a potential fix for k-ω two-equation models, to improve their predictive ability in separation bubble regions. The fix was based on an idea in unpublished work of Volker, Langtry, and Menter that $\mathcal{P}/\varepsilon$ could be used as a trigger to recognize the shear layer of a separation bubble, where increased eddy viscosity might be desired for additional turbulent mixing. The unpublished work used a proprietary methodology, so in the current work a new methodology was "invented" in order to explore the idea independently. The idea was tried within the Menter SST model for a variety of different cases. When using the fix, the boundary layer region was shielded from its effects through the use of a blending function.

Overall, the ad hoc method behaved as expected. The trigger recognized separated shear layers, and a term multiplying the destruction term of the ω-equation caused an increase in eddy viscosity throughout the separated region, reducing the separation bubble size and bringing about flow recovery earlier. The two exceptions to this behavior were the 2-D separated diffuser and the 3-D axisymmetric bump. Here, the $\mathcal{P}/\varepsilon$ levels in the shear layer were too low to trigger the fix to any significant extent, and SST-sf results were essentially identical to SST. However, these two cases are considered to be ones for which SST already yields reasonably good predictions, so the fact that SST-sf produced the same results is encouraging.

As far as improving results compared to LES and experiment, the fix was clearly not universal. It yielded improved results for the 2-D hill and the 2-D

hump (both with no flow control and with steady suction), but it degraded the results for the 2-D backstep, for which SST already worked reasonably well.

An important question that arose out of this study is the following: why do many RANS models (like SST) predict the turbulent shear stress in some separation bubbles like the backstep well, yet severely under-predict this quantity in magnitude in other bubbles like the hill and hump? Presumably in the latter cases the turbulence in the bubble is more energetic. $\mathcal{P}/\varepsilon$ may not be an ideal discriminator for determining whether or not additional eddy viscosity is needed to improve the model.

The separation fix proposed in the current work represents a possible tool that could prove very useful in certain circumstances, but it is not recommended as a permanent model addition for all circumstances. The methodology is simple to understand and implement, easy to trigger on and off inside CFD codes, and yields grid-convergent behavior. Additional RANS work in this area should focus on finding and/or recalibrating the trigger mechanism to be more closely tied to the physics of different types of separation bubbles. If a single model could be devised to work well for all of the cases described here, it would represent a significant breakthrough for RANS turbulence modeling.

References

1. Rumsey, C. L., "Successes and Challenges for Flow Control Simulations," *International Journal of Flow Control*, Vol. 1, No. 1, 2009, pp. 1–27.

2. Rumsey, C. L., "Effect of Turbulence Models on Two Massively-Separated Benchmark Flow Cases," NASA/TM-2003-212412, May 2003.

3. Wilcox, D. W., *Turbulence Modeling For CFD*, 3rd ed., DCW Industries, La Canada, 2006.

4. Rumsey, C. L., "Reynolds-Averaged Navier-Stokes Analysis of Zero Efflux Flow Control over a Hump Model," *Journal of Aircraft*, Vol. 44, No. 2, 2007, pp. 444–452.

5. Menter, F. R., "Two-Equation Eddy-Viscosity Turbulence Models for Engineering Applications," *AIAA Journal*, Vol. 32, No. 8, 1994, pp. 1598–1605.

6. Menter, F. R., "Improved Two-Equation k-omega Turbulence Models for Aerodynamic Flows," NASA TM 103975, October 1992.

7. Bradshaw, P., Ferriss, D. H., and Atwell, N. P., "Calculation of Boundary-Layer Development Using the Turbulent Energy Equation," *J. Fluid Mech.*, Vol. 28, Part 3, 1967, pp. 593–616.

8. Spalart, P. R., Deck, S., Shur, M. L., Squires, K. D., Strelets, M. Kh., and Travin, A., "A New Version of Detached-Eddy Simulation, Resistant to Ambiguous Grid Densities," *Theor. Comput. Fluid Dyn.*, Vol. 20, 2006, pp. 181–195.

9. Hellsten, A., "Some Improvements in Menter's k-ω SST Turbulence Model," AIAA Paper 98-2554, June 1998.

10. Mani, M., Ladd, J. A., and Bower, W. W., "Rotation and Curvature Correction Assessment for One- and Two-Equation Turbulence Models," *Journal of Aircraft*, Vol. 41, No. 2, 2004, pp. 268–273.

11. Krist, S. L., Biedron, R. T., and Rumsey, C. L., "CFL3D User's Manual (Version 5.0)," NASA TM-1998-208444, June 1998.

12. Weiss, J. M. and Smith, W. A., "Preconditioning Applied to Variable and Constant Density Flows," *AIAA Journal*, Vol. 33, No. 11, 1995, pp. 2050–2057.

13. Roe, P. L., "Approximate Riemann Solvers, Parameter Vectors, and Difference Schemes," *J. Computational Physics*, Vol. 43, 1981, pp. 357–372.

14. Almeida, G. P., Durao, D. F. G., and Heitor, M. V., "Wake Flows Behind Two Dimensional Model Hills," *Exp. Thermal and Fluid Science*, Vol. 7, 1993, pp. 87–101.

15. Jang, Y. J., Temmerman, L., and Leschziner, M. A., "Investigation of Anisotropy-Resolving Turbulence Models by Reference to Highly-Resolved LES Data for Separated Flows," ECCOMAS Computational Fluid Dynamics Conference 2001, Swansea, Wales.

16. Manceau, R., Bonnet, J.-P., Leschziner, M. A., and Menter, F. (eds.), *Proceedings of the 10th Joint ERCOFTAC (SIG-15) / IAHR / QNET-CFD Workshop on Refined Turbulence Modelling*, CNRS / Universite de Poitiers, France, October 10–11, 2002.

17. Spalart, P. R. and Allmaras, S. R., "A One-Equation Turbulence Model for Aerodynamic Flows," *Recherche Aerospatiale*, No. 1, 1994, pp. 5–21.

18. Rumsey, C. L. and Thomas, J. L., "Application of FUN3D and CFL3D to the Third Workshop on CFD Uncertainty Analysis," NASA/TM-2008-215537, November 2008.

19. Driver, D. M. and Seegmiller, H. L., "Features of a Reattaching Turbulent Shear Layer in Divergent Channel Flow," *AIAA Journal*, Vol. 23, No. 2, 1985, pp. 163–171.

20. Monson, D. J., Seegmiller, H. L., McConnaughey, P. K., and Chen, Y. S., "Comparison of Experiment with Calculations Using Curvature-Corrected Zero and Two-Equation Turbulence Models for a Two-Dimensional U-Duct," AIAA Paper 90-1484, June 1990.

21. Obi, S., Aoki, K., and Masuda, S., "Experimental and Computational Study of Separating Flow in an Axisymmetric Planar Diffuser," 9th Symposium on Turbulent Shear Flows, Kyoto, Japan, 1993, pp. 305.1–305.4.

22. Buice, C. U. and Eaton, J. K., "Experimental Investigation of Flow through an Axisymmetric Plane Diffuser," *Journal of Fluids Engineering*, Vol. 122, June 2000, pp. 433–435.

23. Hirsch, C. and Tartinville, B., "Reynolds-Averaged Navier-Stokes Modelling for Industrial Applications and Some Challenging Issues," *Int J. of Computational Fluid Dynamics*, Vol. 23, No. 4, 2009, pp. 295–303.

24. Kaltenbach, H.-J., Fatica, M., Mittal, R., Lund, T. S., and Moin, P., "Study of Flow in a Planar Axisymmetric Diffuser Using Large-Eddy Simulation," *Journal of Fluid Mechanics*, Vol. 390, 1999, pp. 151–185.

25. Seifert, A. and Pack, L. G., "Active Flow Separation Control on Wall-Mounted Hump at High Reynolds Numbers," *AIAA Journal*, Vol. 40, No. 7, 2002, pp. 1363–1372.

26. Greenblatt, D., Paschal, K. B., Yao, C.-S., Harris, J., Schaeffler, N. W., and Washburn, A. E., "Experimental Investigation of Separation Control Part 1: Baseline and Steady Suction," *AIAA Journal*, Vol. 44, No. 12, 2006, pp. 2820–2830.

27. Greenblatt, D., Paschal, K. B., Yao, C.-S., and Harris, J., "Experimental Investigation of Separation Control Part 2: Zero Mass-Efflux Oscillatory Blowing," *AIAA Journal*, Vol. 44, No. 12, 2006, pp. 2831–2845.

28. Rumsey, C. L., Gatski, T. B., Sellers, W. L., III, Vatsa, V. N., and Viken, S. A., "Summary of the 2004 Computational Fluid Dynamics Validation Workshop on Synthetic Jets," *AIAA Journal*, Vol. 44, No. 2, 2006, pp. 194–207.

29. Bachalo, W. D. and Johnson, D. A., "Transonic, Turbulent Boundary-Layer Separation Generated on an Axisymmetric Flow Model," *AIAA Journal*, Vol. 24, No. 3, March 1986, pp. 437–443.

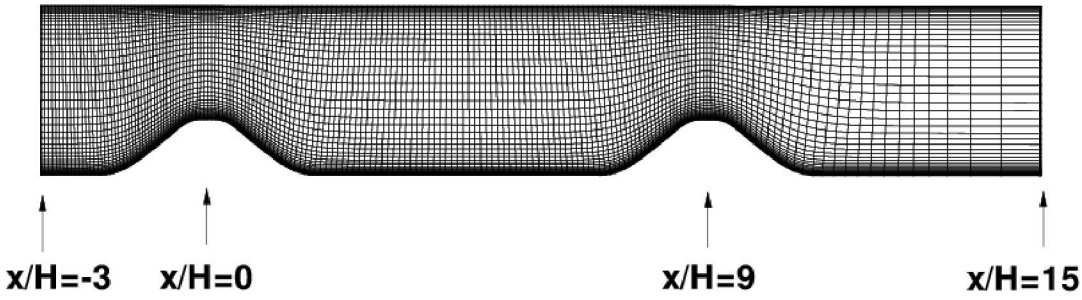

Figure 1. 737 × 193 2-D hill grid, with every fourth gridpoint shown.

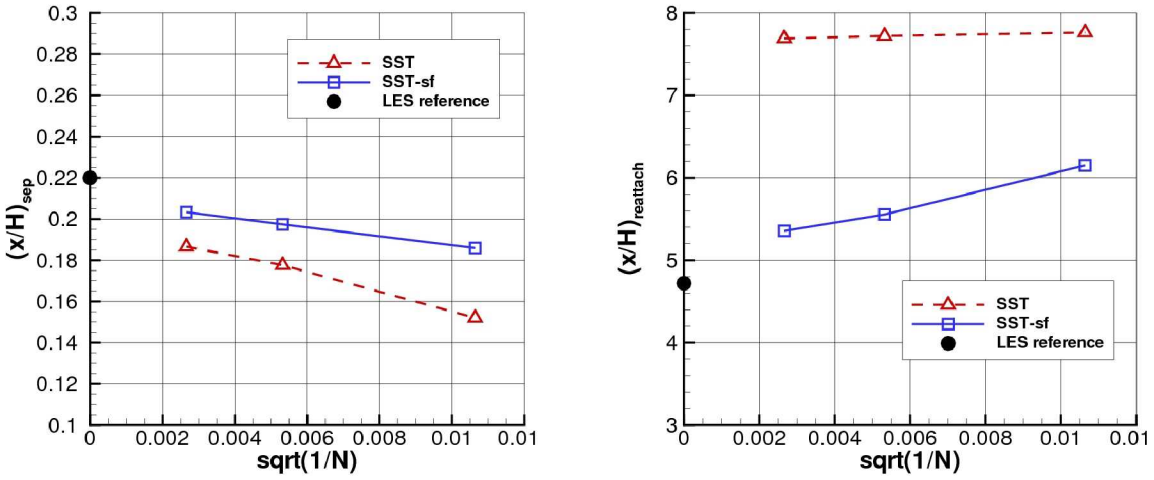

Figure 2. Separation and reattachment locations for the 2-D hill.

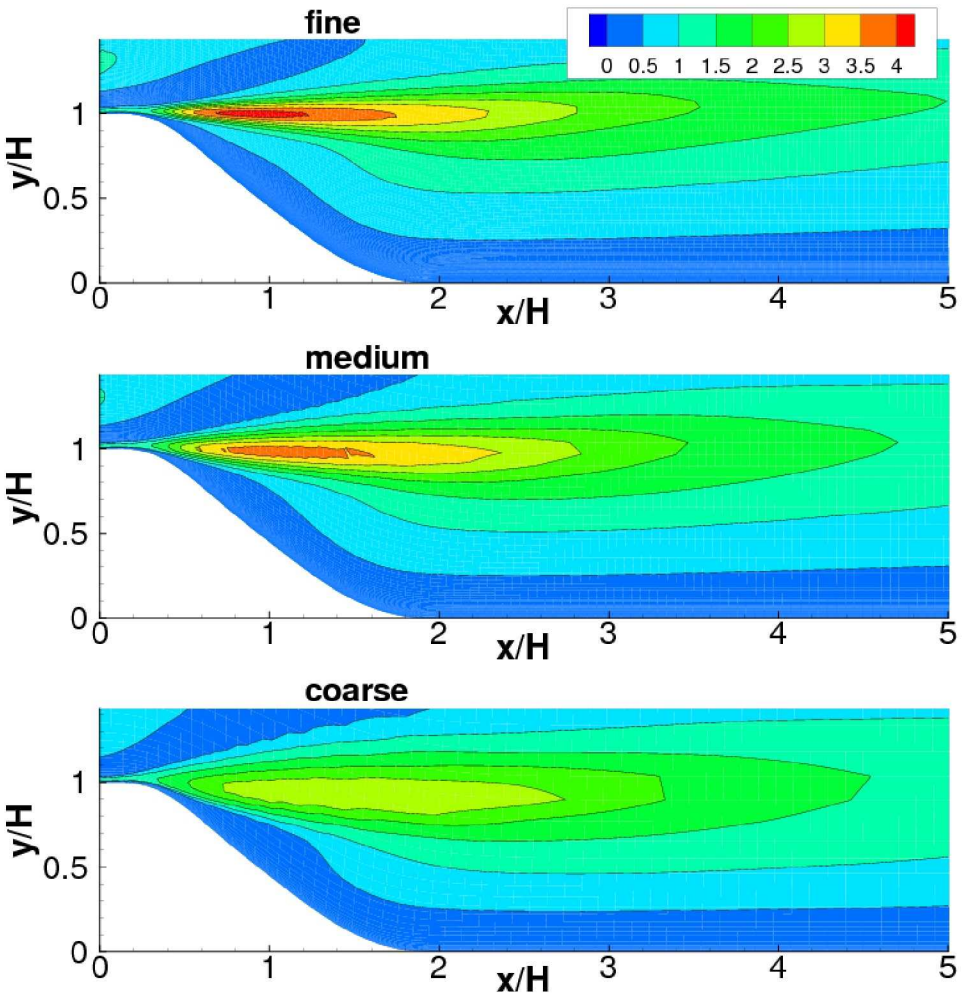

Figure 3. Contours of $\mathcal{P}/\varepsilon$ on three different grid sizes for the 2-D hill.

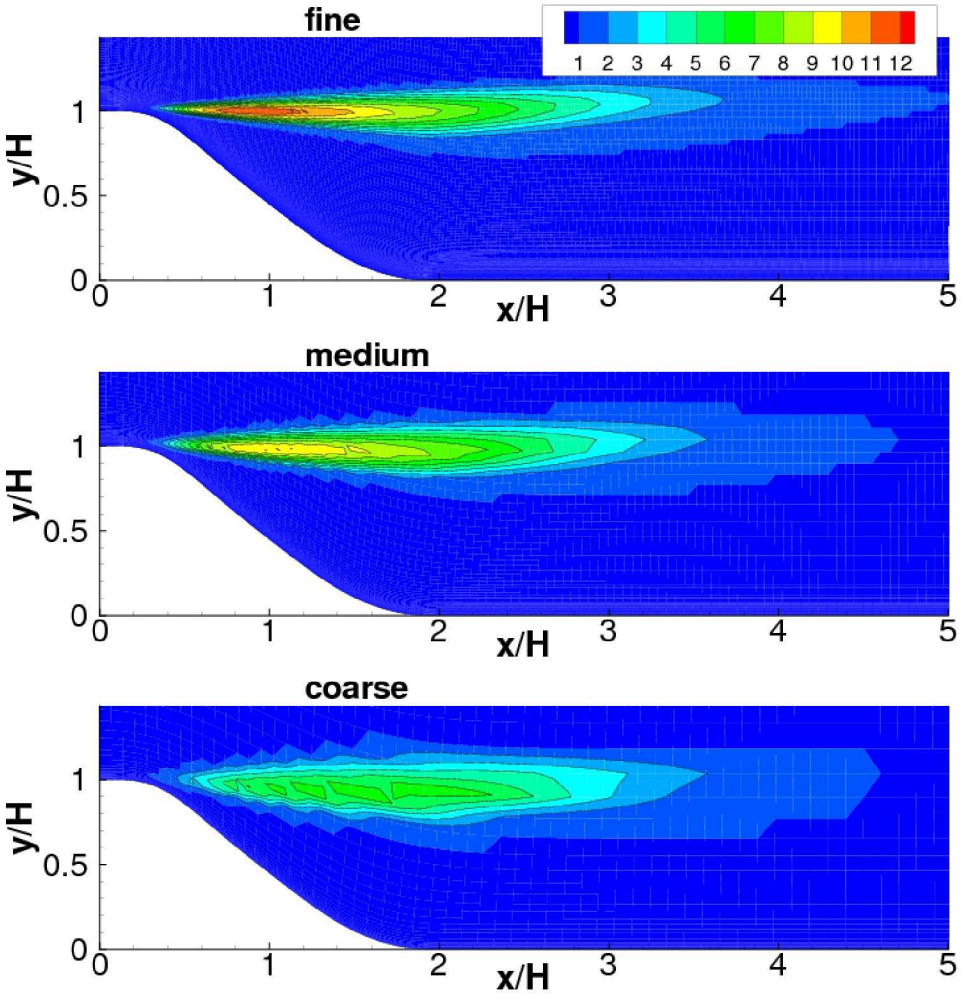

Figure 4. Contours of F_{sf} on three different grid sizes for the 2-D hill; SST-sf model.

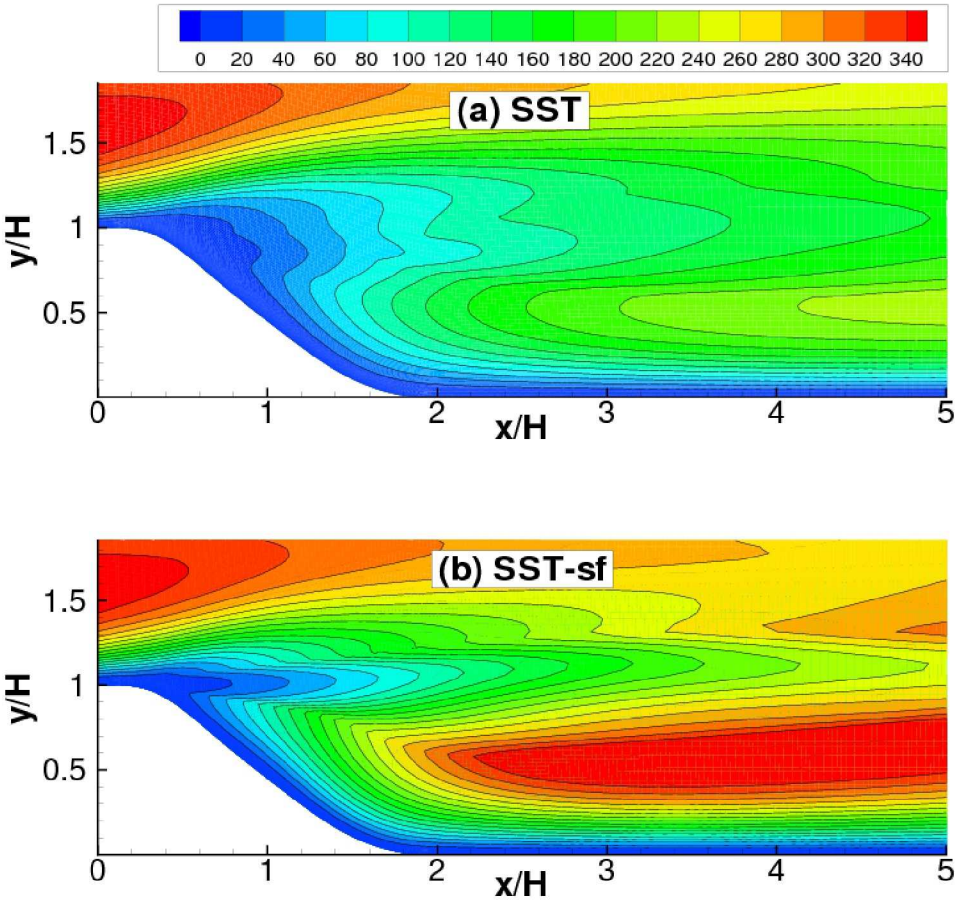

Figure 5. Contours of eddy viscosity (μ_t) for the 2-D hill (fine grid); (a) SST, (b) SST-sf.

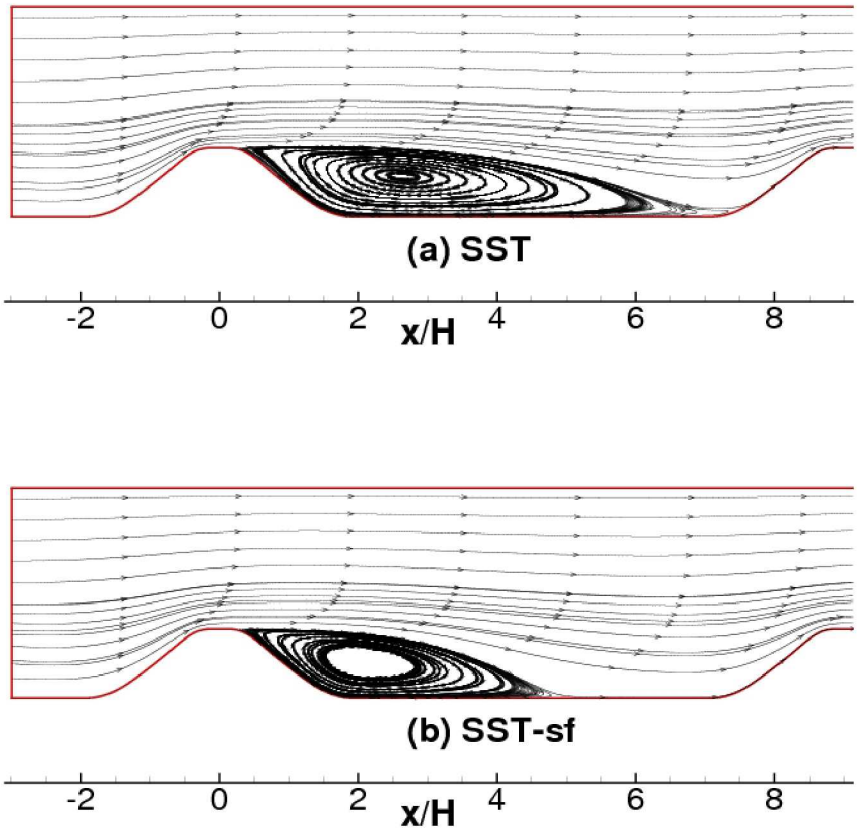

Figure 6. Streamlines for the 2-D hill (fine grid); (a) SST, (b) SST-sf.

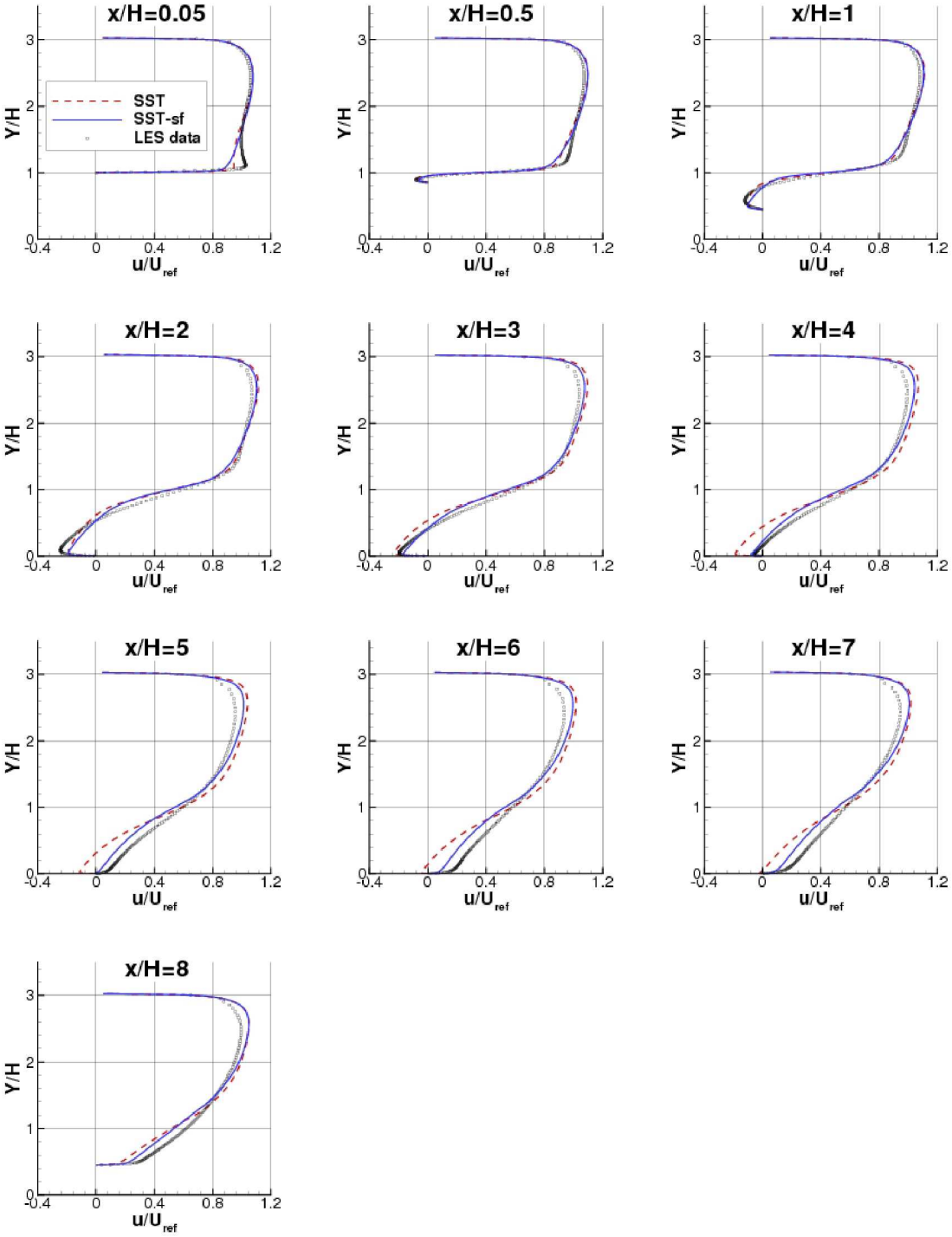

Figure 7. 2-D hill velocity profiles (RANS results on fine grid).

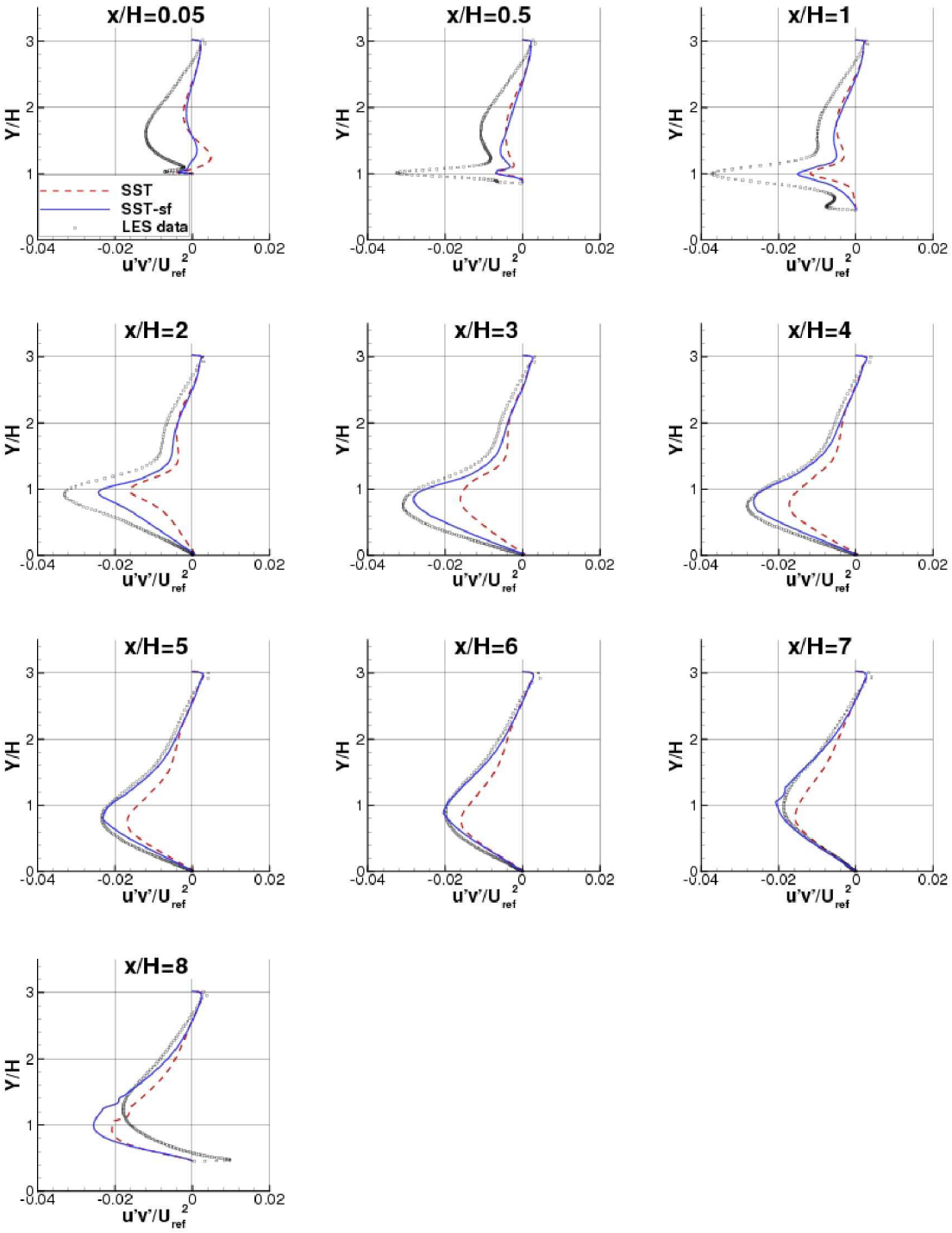

Figure 8. 2-D hill turbulent shear stress profiles (RANS results on fine grid).

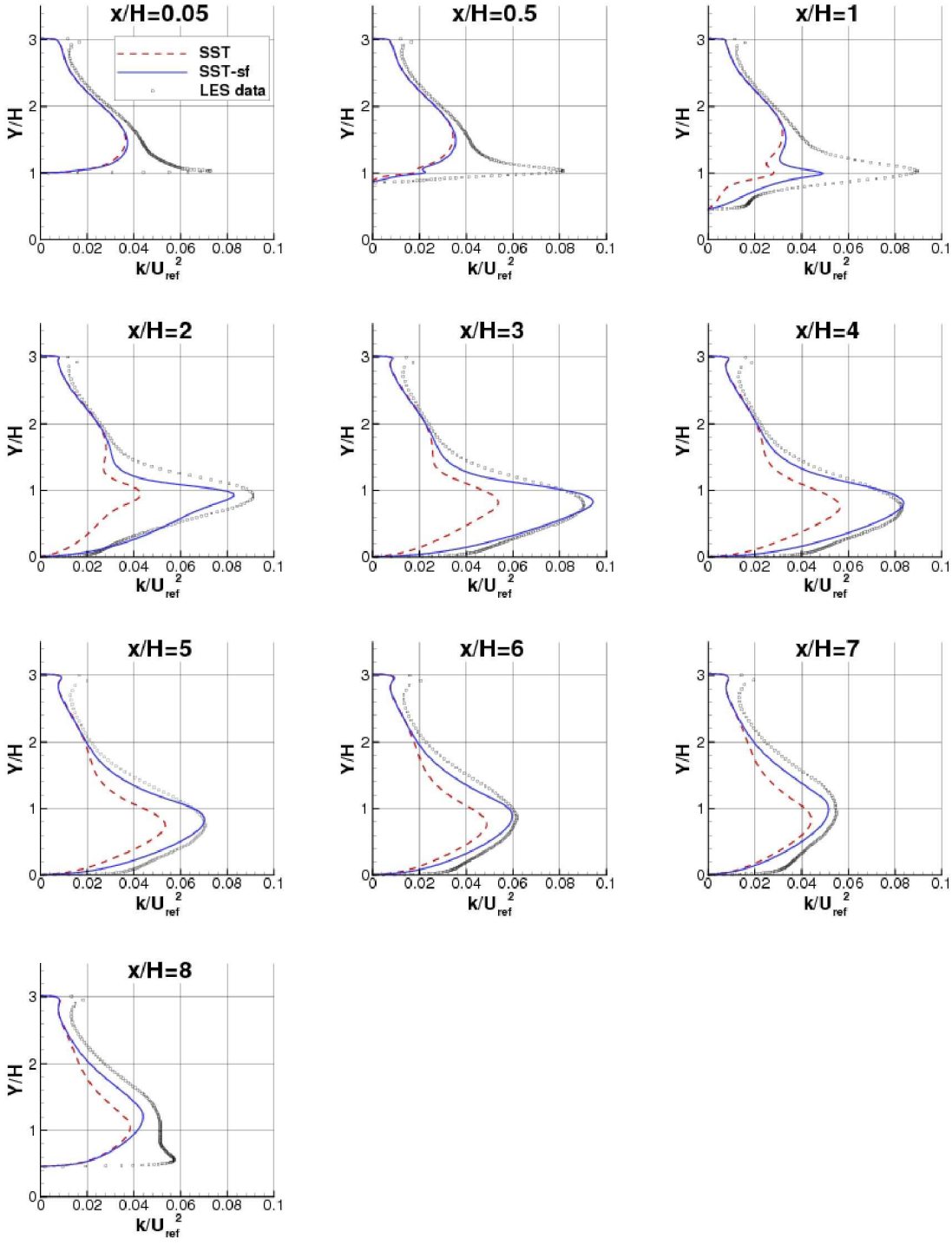

Figure 9. 2-D hill turbulent kinetic energy profiles (RANS results on fine grid).

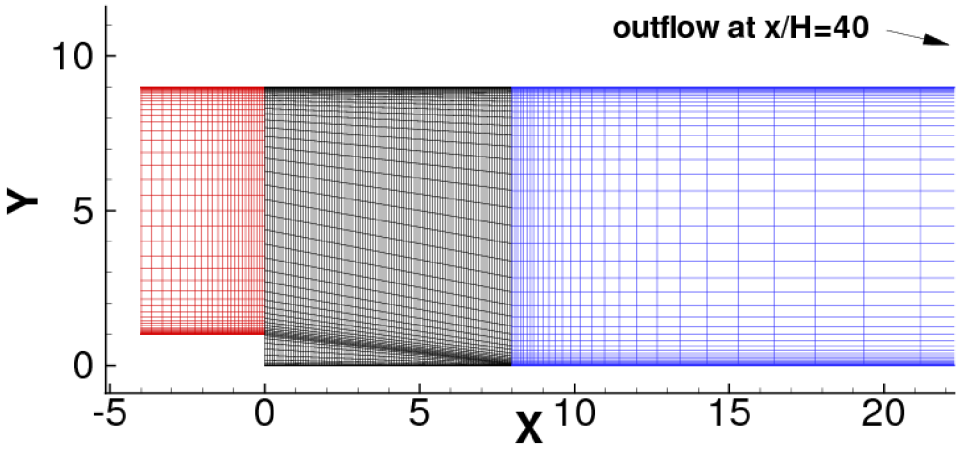

Figure 10. 2-D backstep grid (3 zones: 97 × 257, 385 × 257, and 129 × 257), with every fourth gridpoint shown.

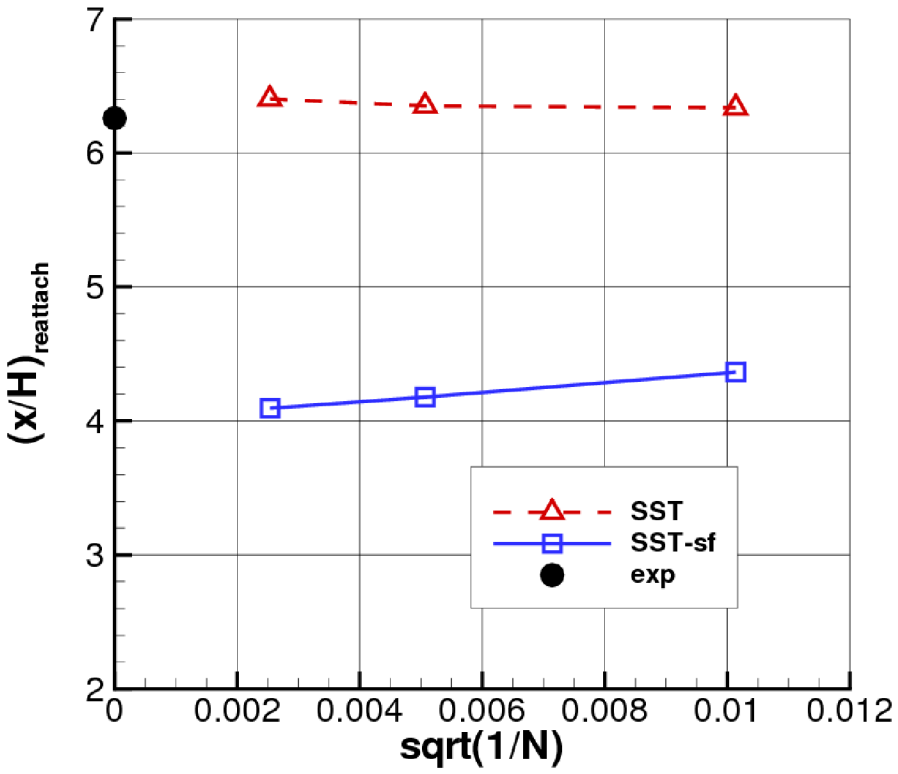

Figure 11. Reattachment locations for the 2-D backstep.

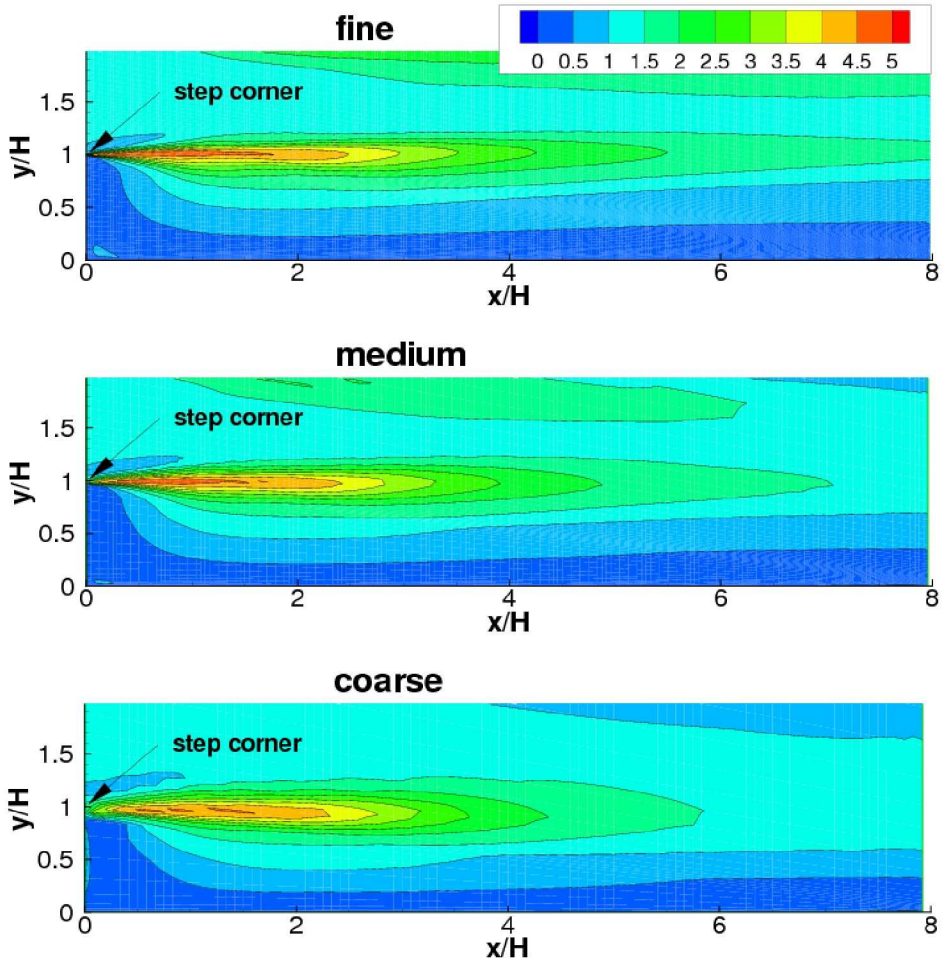

Figure 12. Contours of $\mathcal{P}/\varepsilon$ on three different grid sizes for the 2-D backstep.

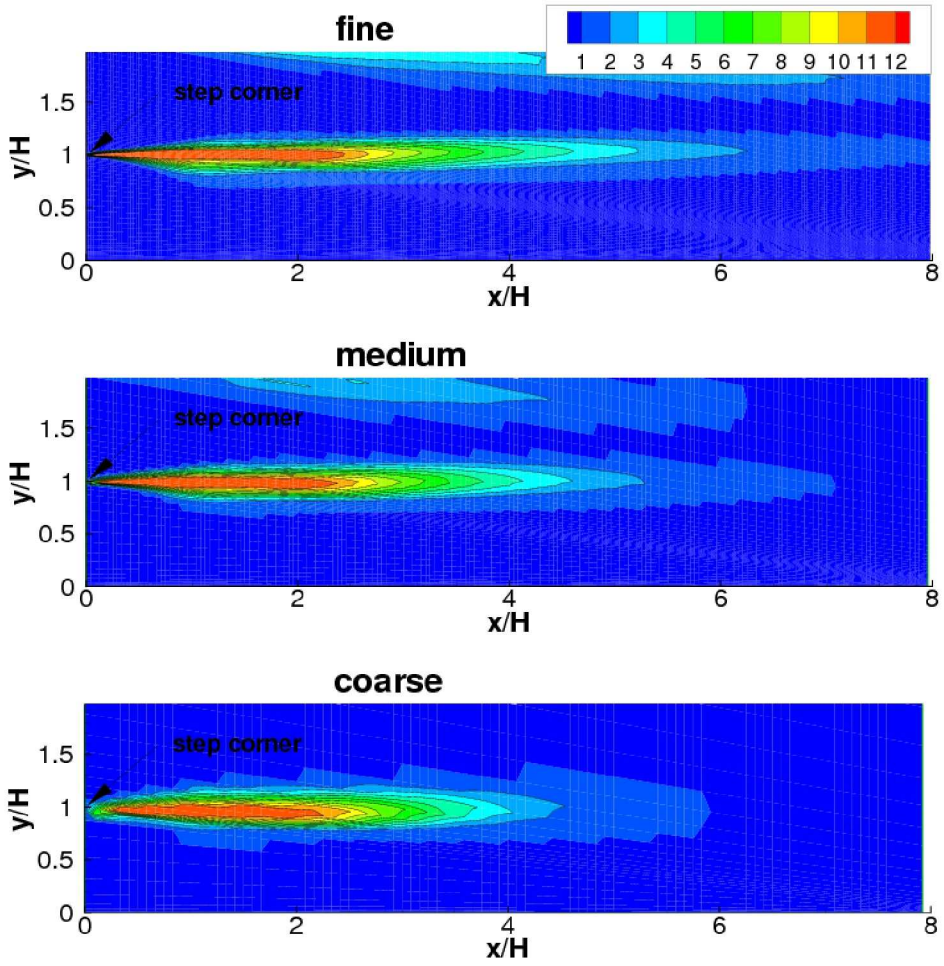

Figure 13. Contours of F_{sf} on three different grid sizes for the 2-D backstep; SST-sf model.

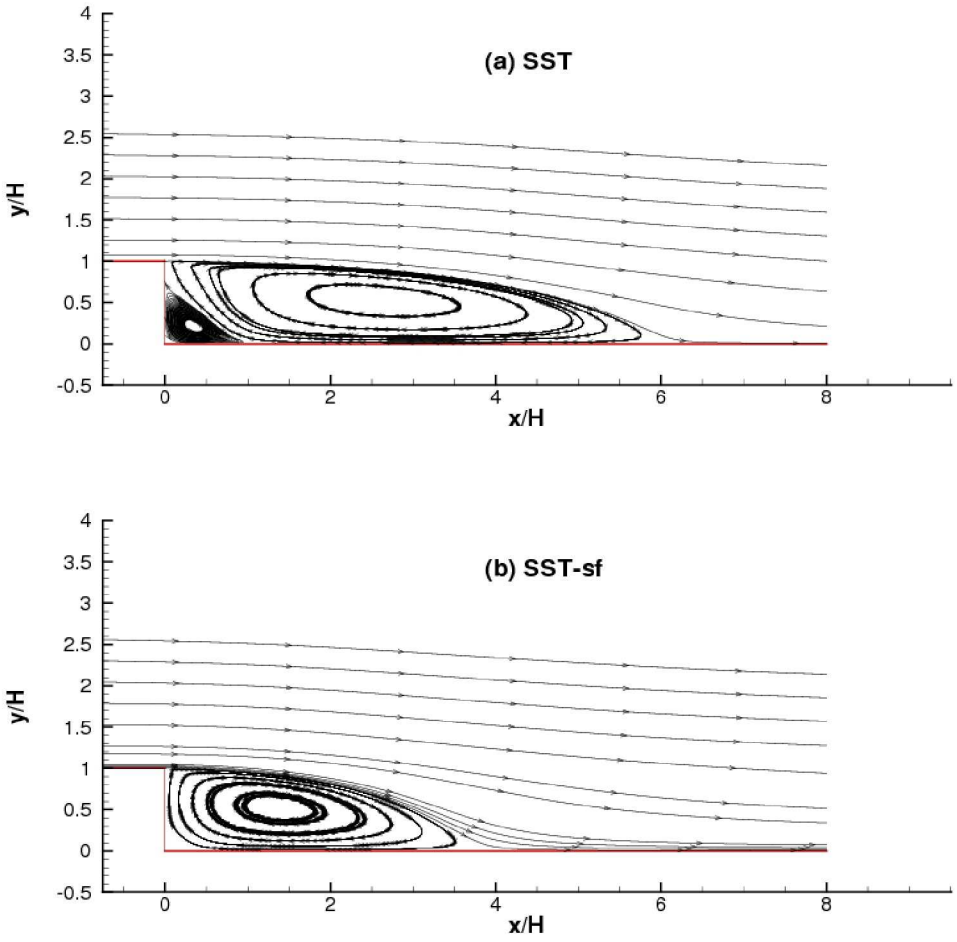

Figure 14. Streamlines for the 2-D backstep (fine grid); (a) SST, (b) SST-sf.

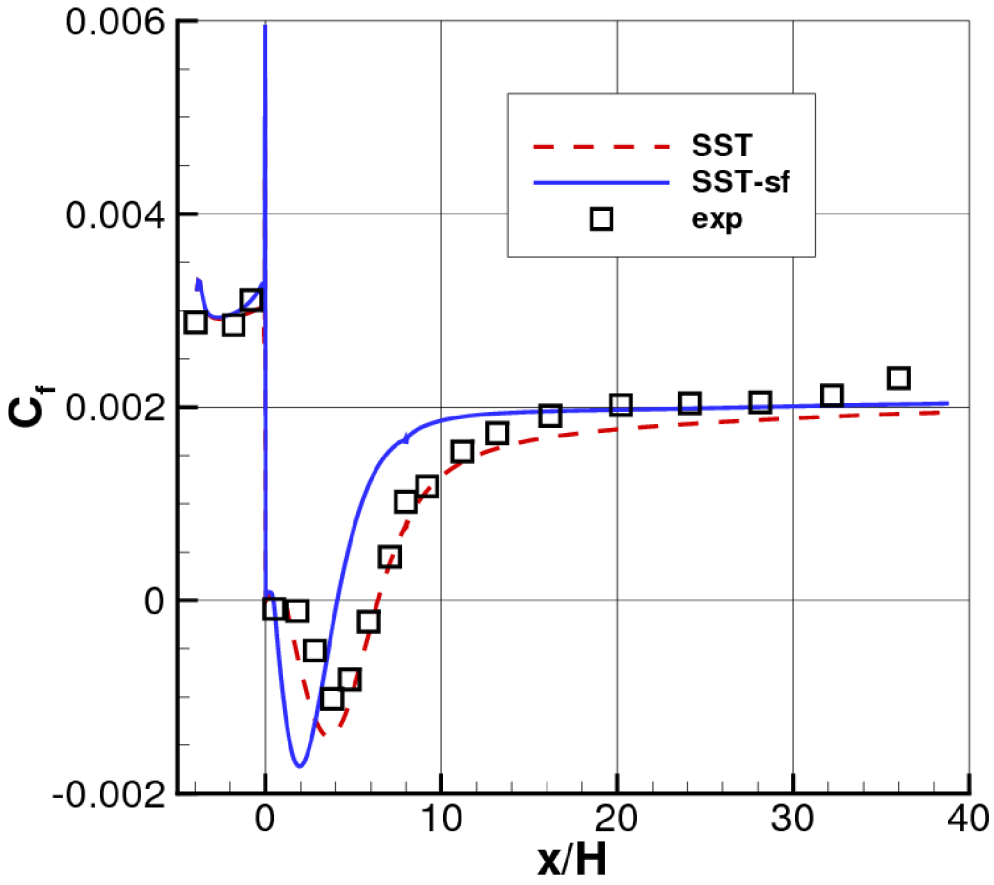

Figure 15. Skin friction coefficient for the 2-D backstep along the bottom wall (fine grid).

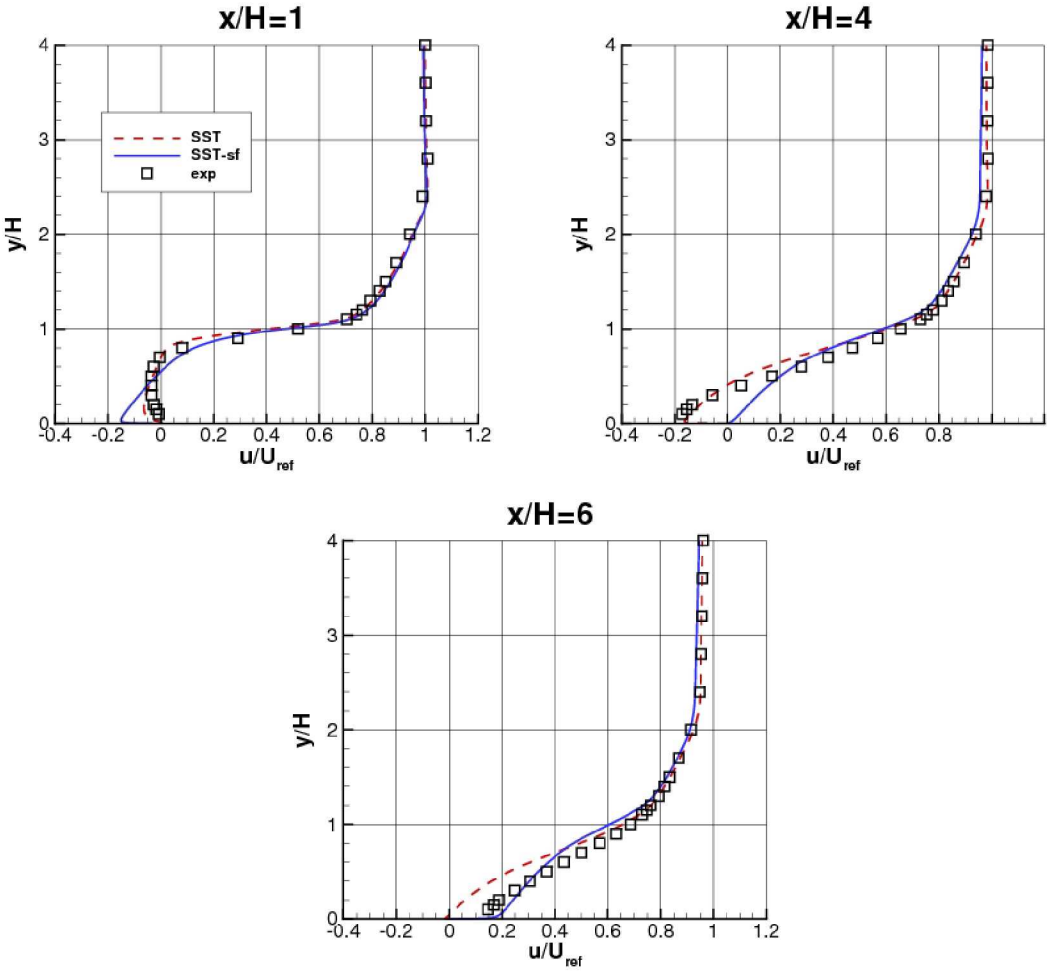

Figure 16. Horizontal velocity profiles for the 2-D backstep (fine grid).

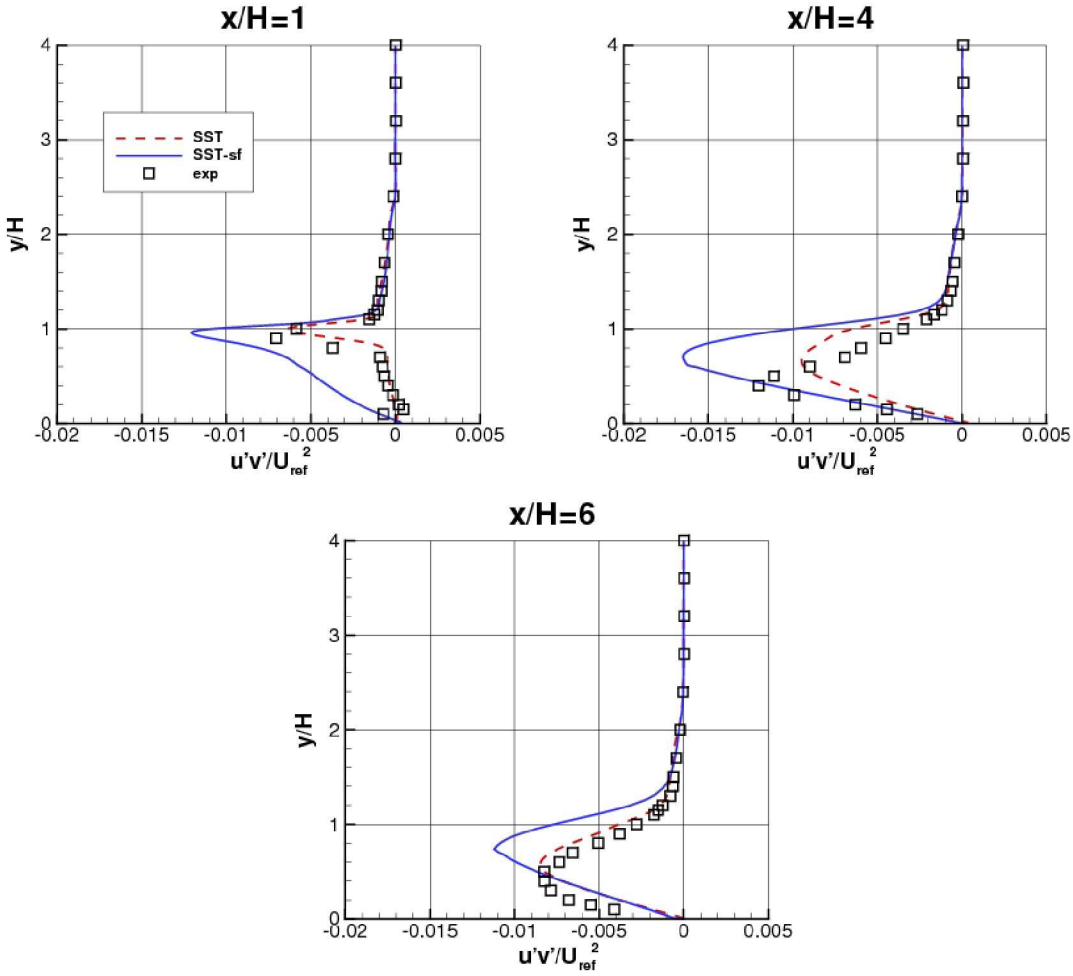

Figure 17. Turbulent shear stress profiles for the 2-D backstep (fine grid).

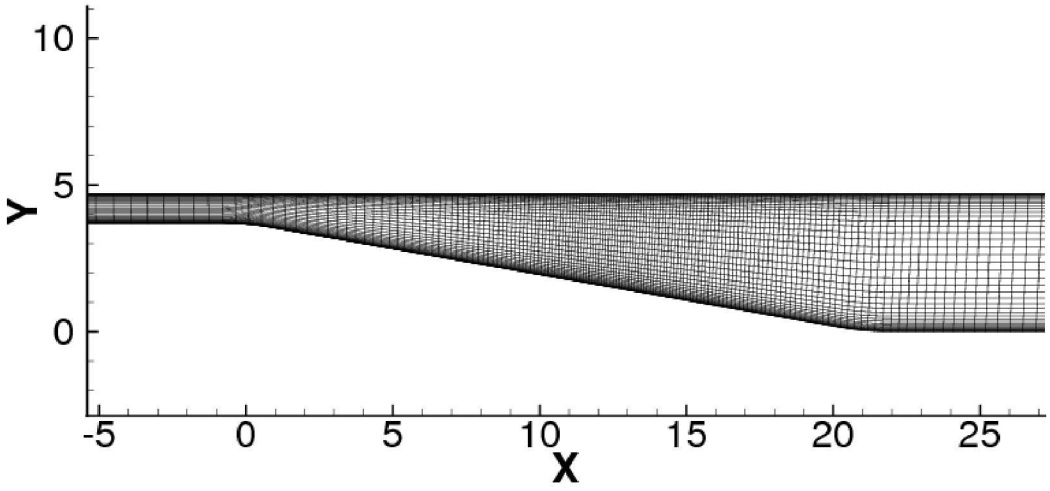

Figure 18. Portion of 865 × 193 2-D diffuser grid, with every fourth gridpoint shown.

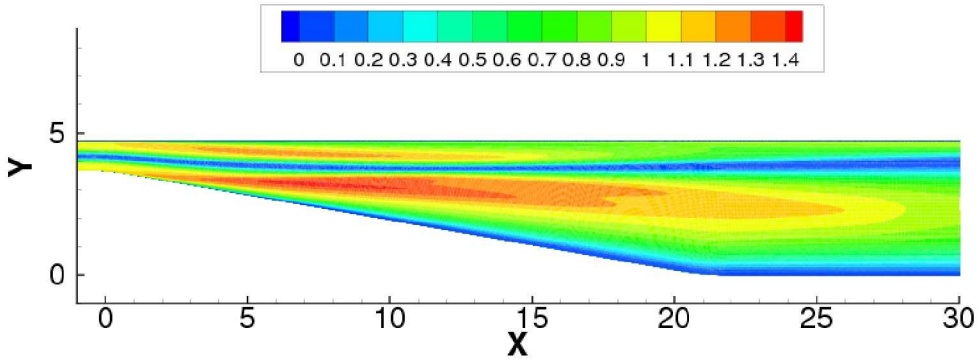

Figure 19. Contours of $\mathcal{P}/\varepsilon$ on the 2-D diffuser (fine grid).

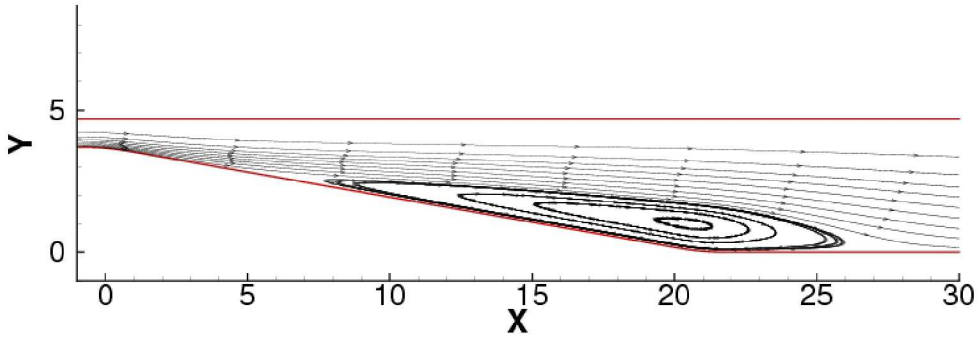

Figure 20. Streamlines for the the 2-D diffuser (fine grid); results are identical for both SST and SST-sf.

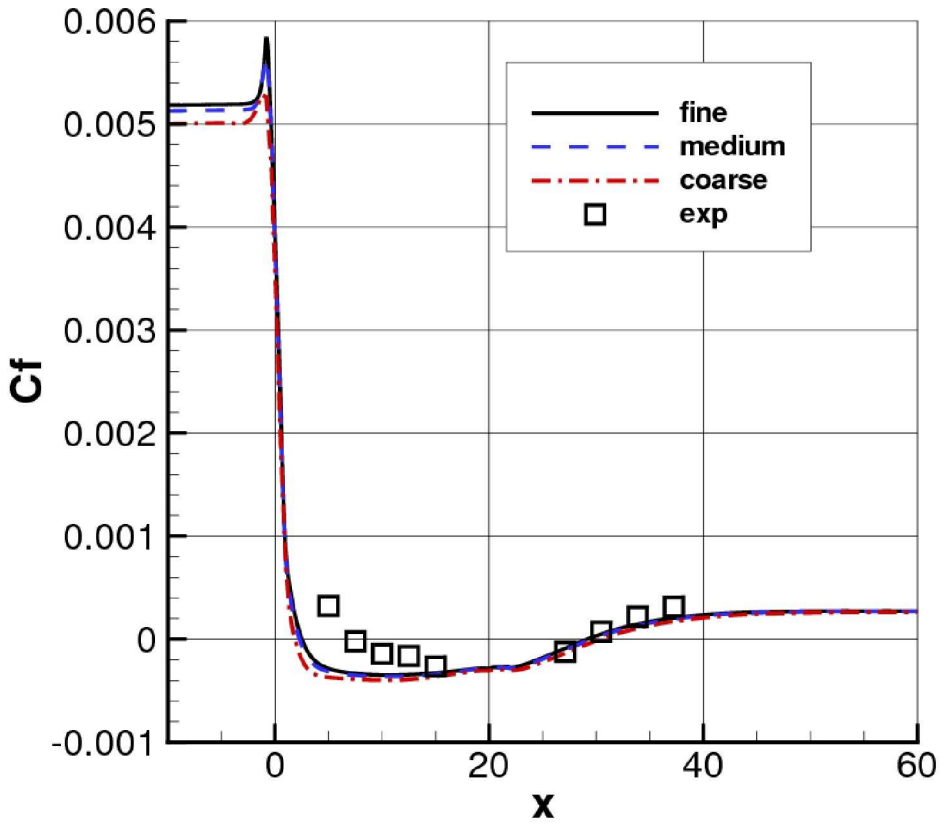

Figure 21. Skin friction coefficient for the 2-D diffuser along the bottom wall (results are identical for both SST and SST-sf).

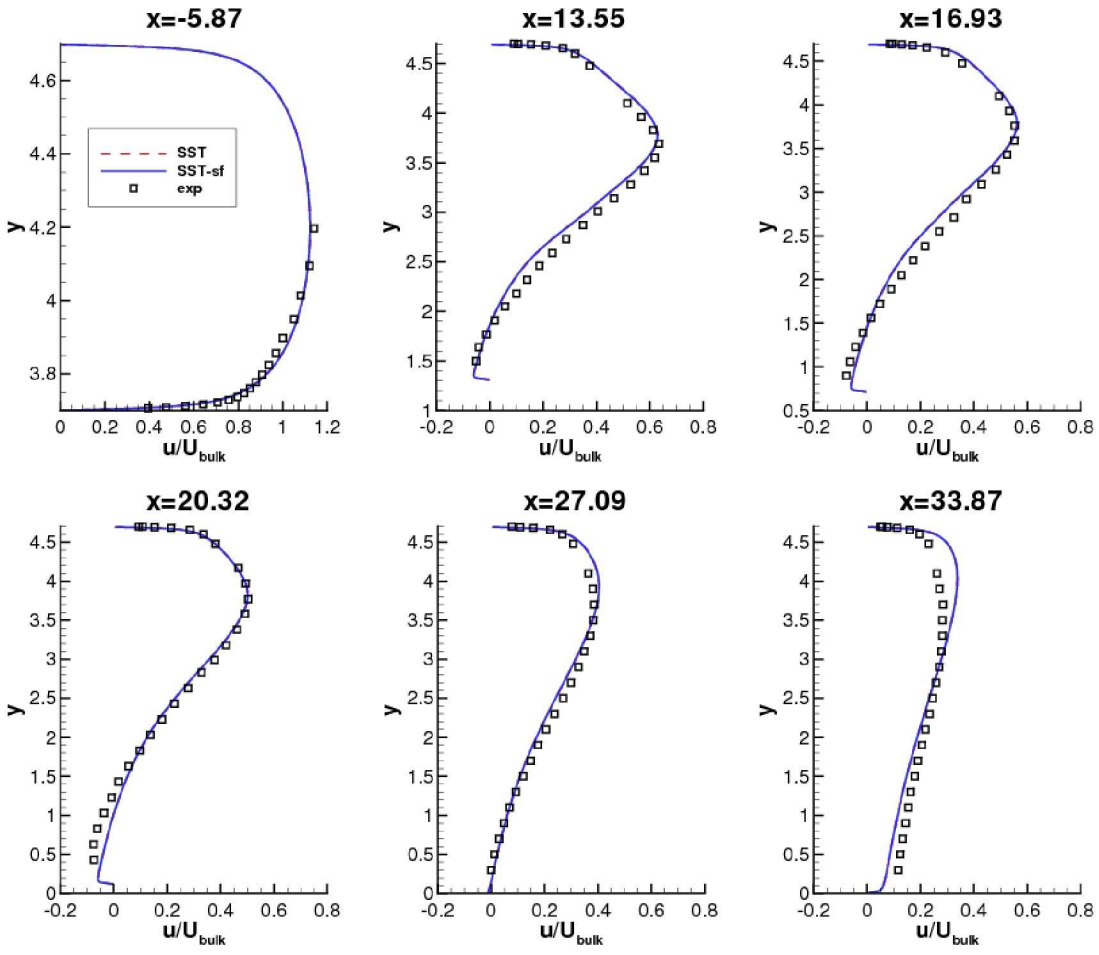

Figure 22. Horizontal velocity profiles for the 2-D diffuser (fine grid).

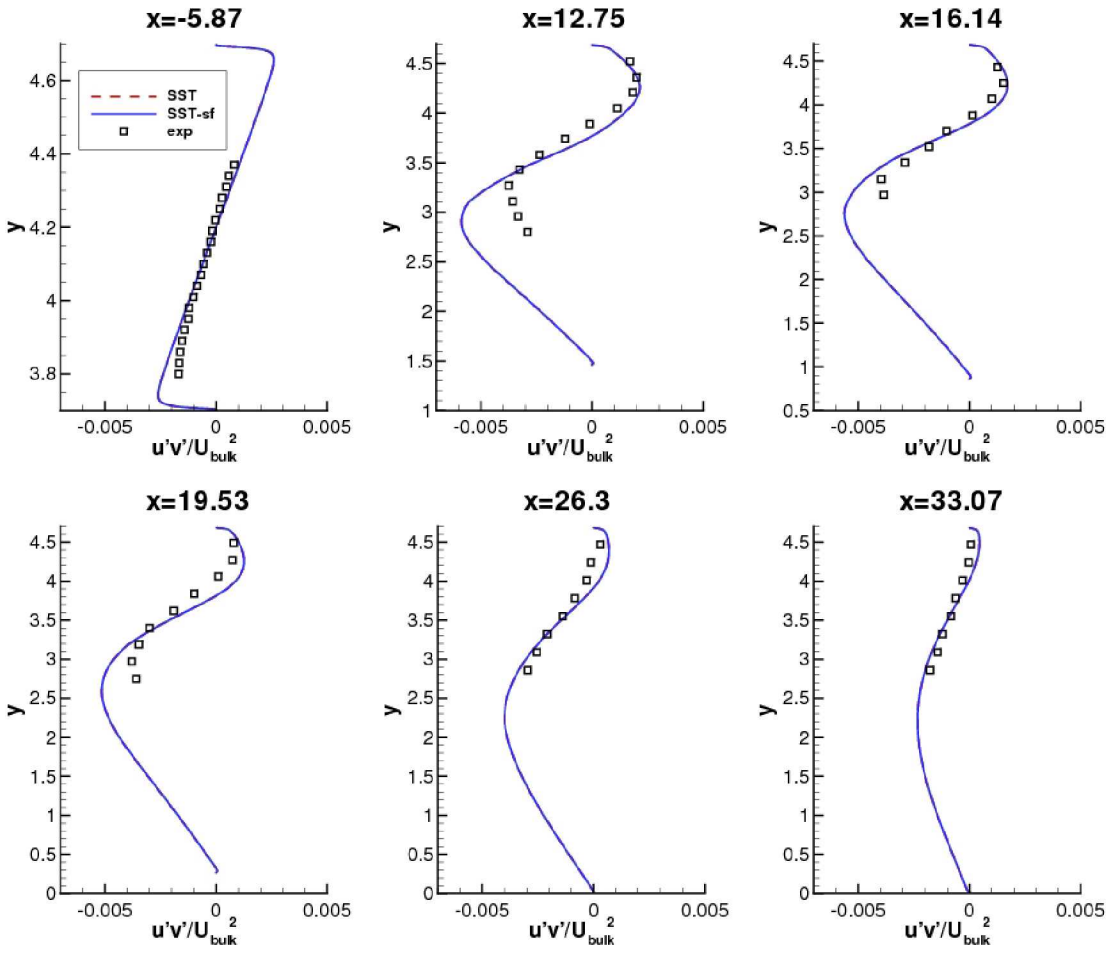

Figure 23. Turbulent shear stress profiles for the 2-D diffuser (fine grid).

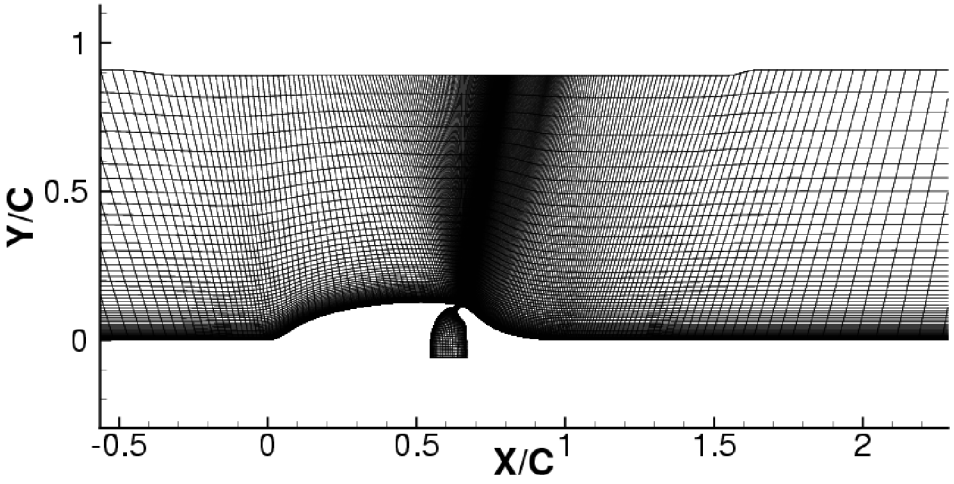

Figure 24. Portion of 2-D hump grid (4 zones: 793×217, 161×121, 65×121, 49×217), with every other gridpoint shown.

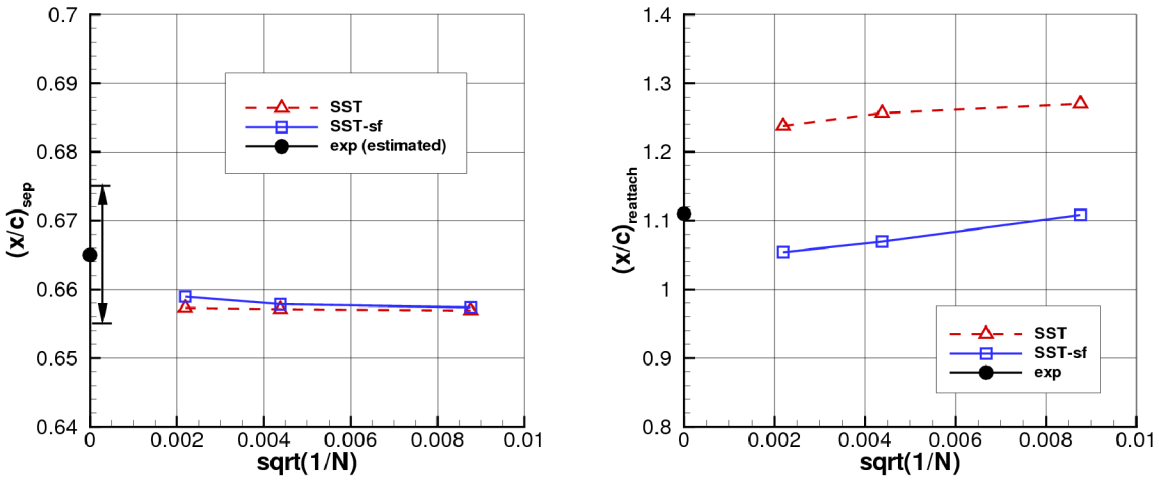

Figure 25. Separation and reattachment locations for the 2-D hump, no flow control.

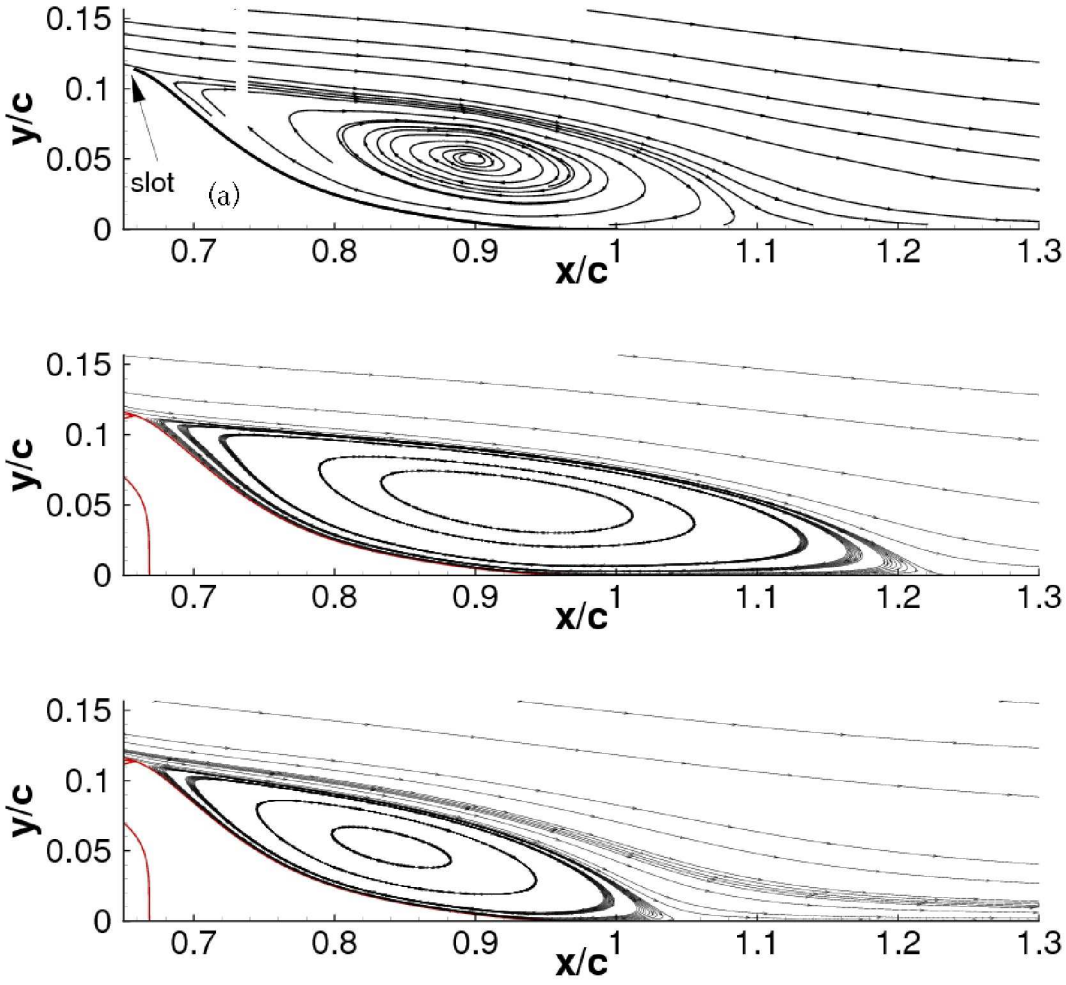

Figure 26. Streamlines for the 2-D hump, no flow control (fine grid); (a) experiment, (b) SST, (c) SST-sf.

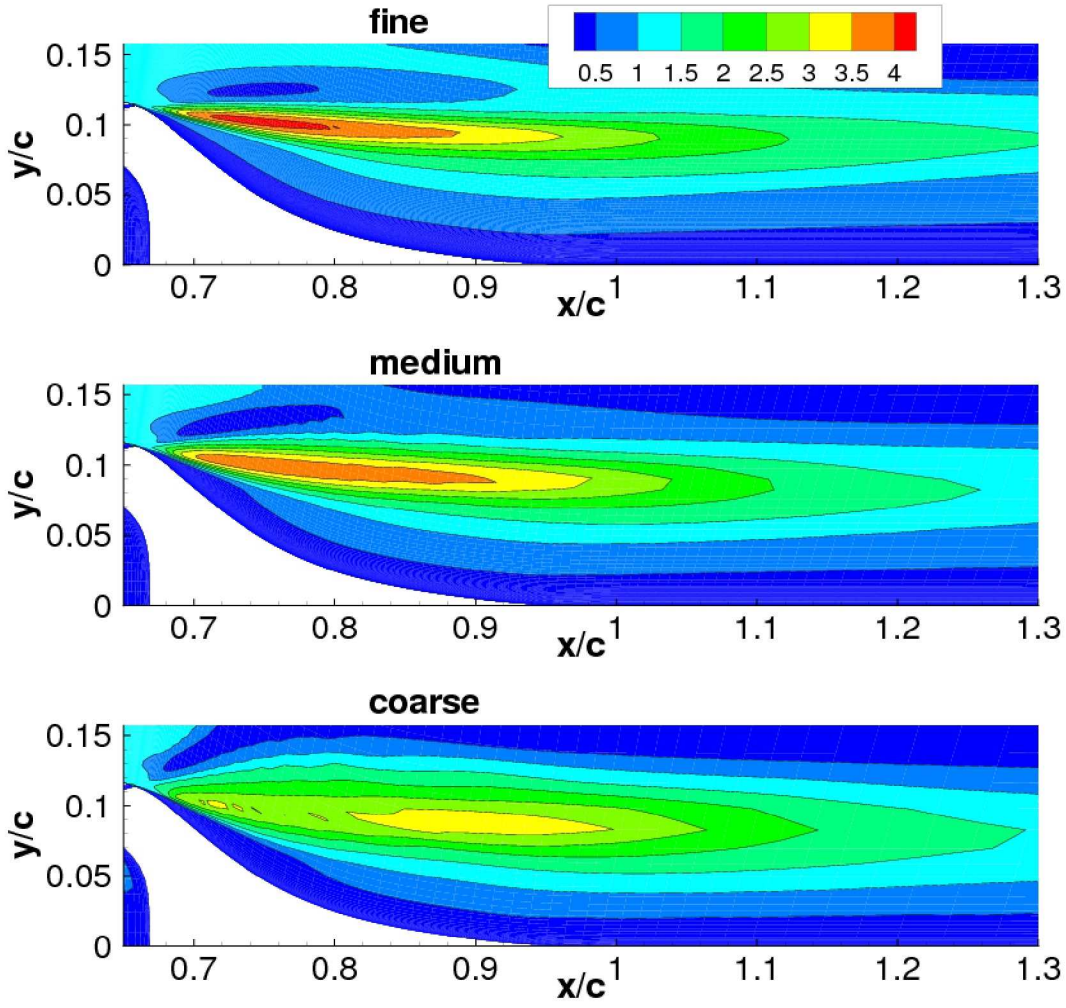

Figure 27. Contours of $\mathcal{P}/\varepsilon$ on three different grid sizes for the 2-D hump, no flow control.

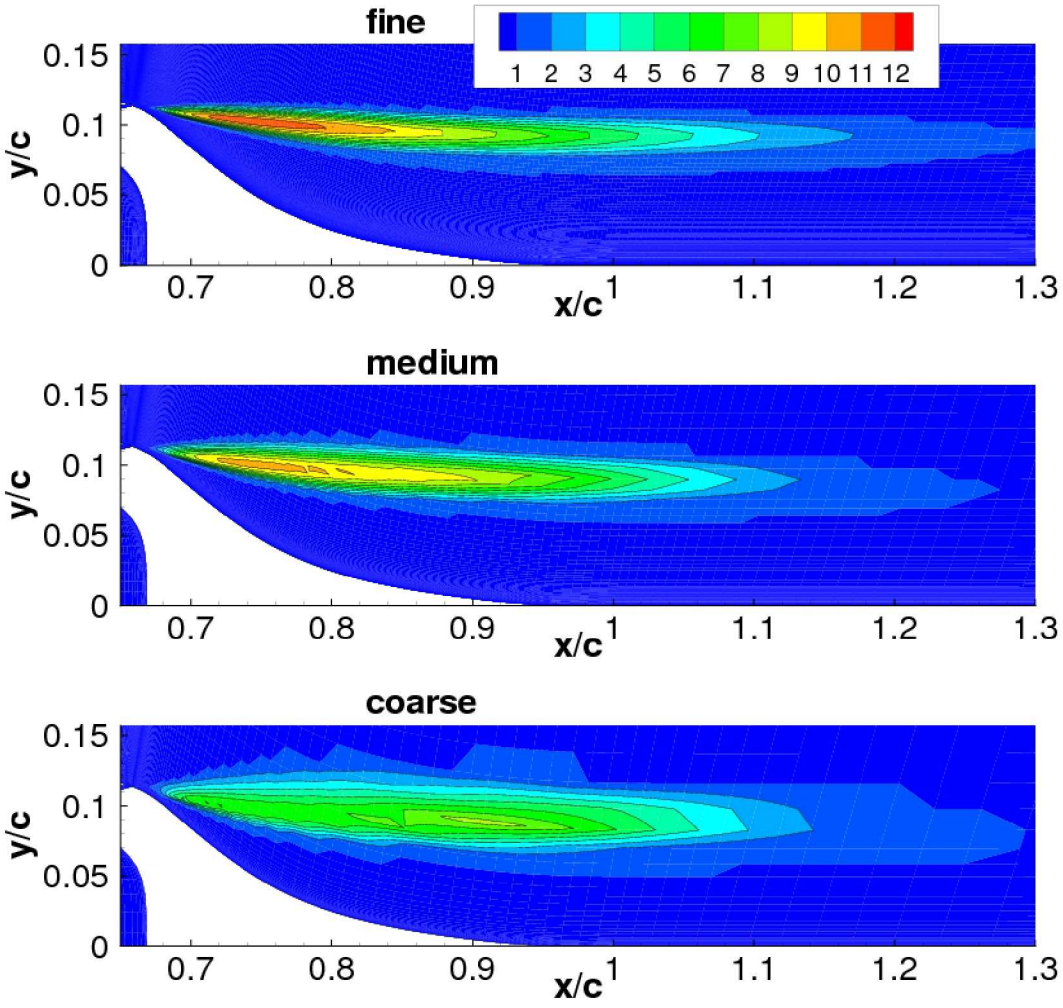

Figure 28. Contours of F_{sf} on three different grid sizes for the 2-D hump, no flow control; SST-sf model.

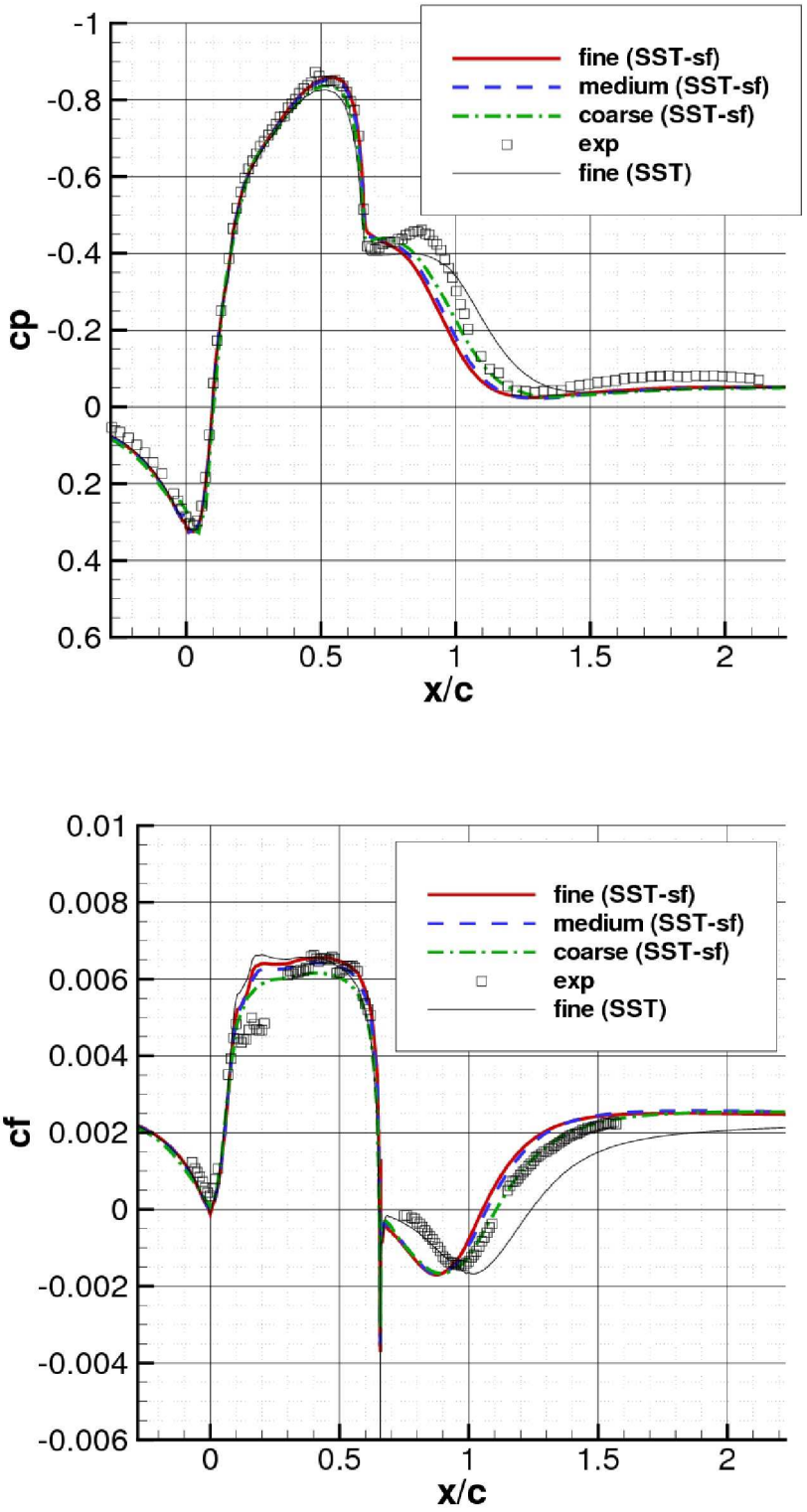

Figure 29. 2-D hump no flow control results; (a) surface pressure coefficient, (b) surface skin friction coefficient.

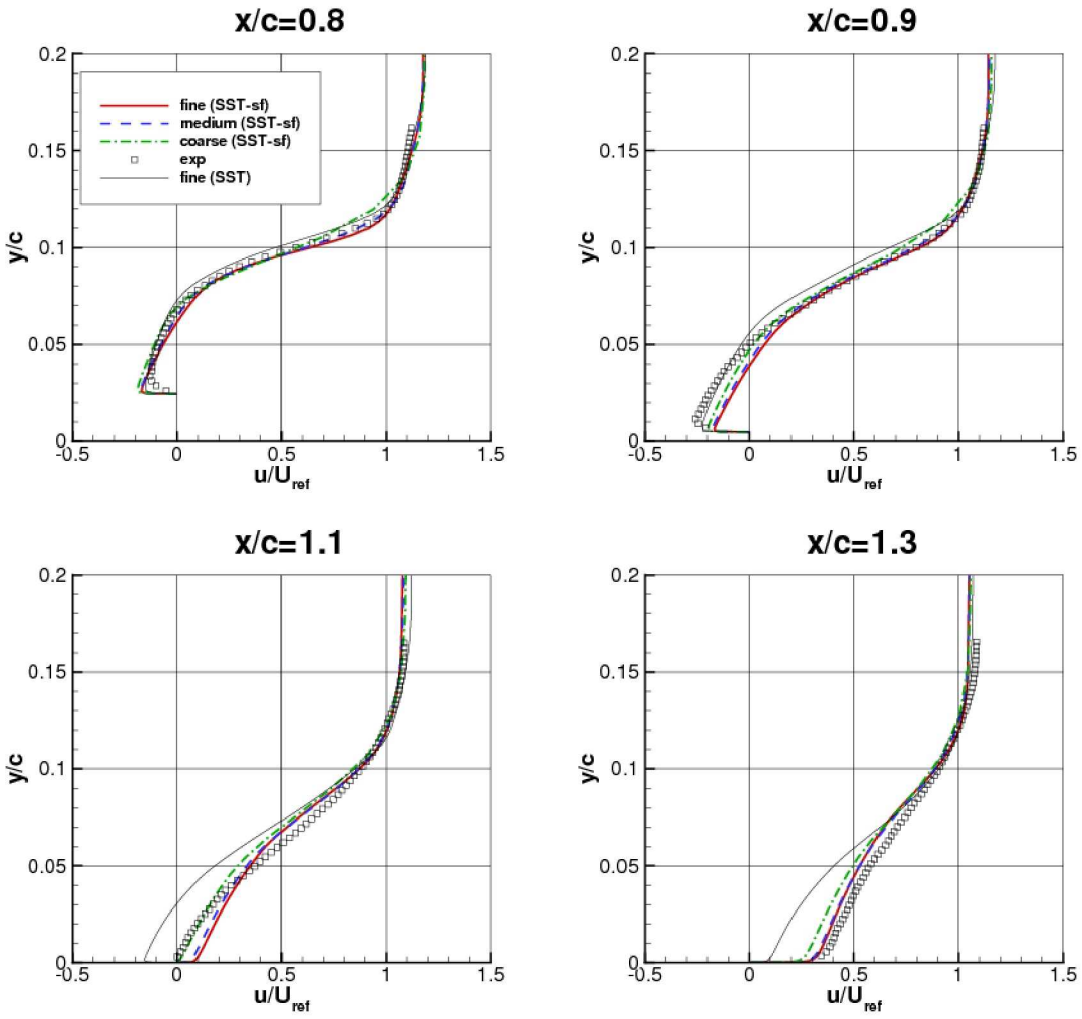

Figure 30. Profiles of horizontal velocity component at four stations on the 2-D hump grid, no flow control.

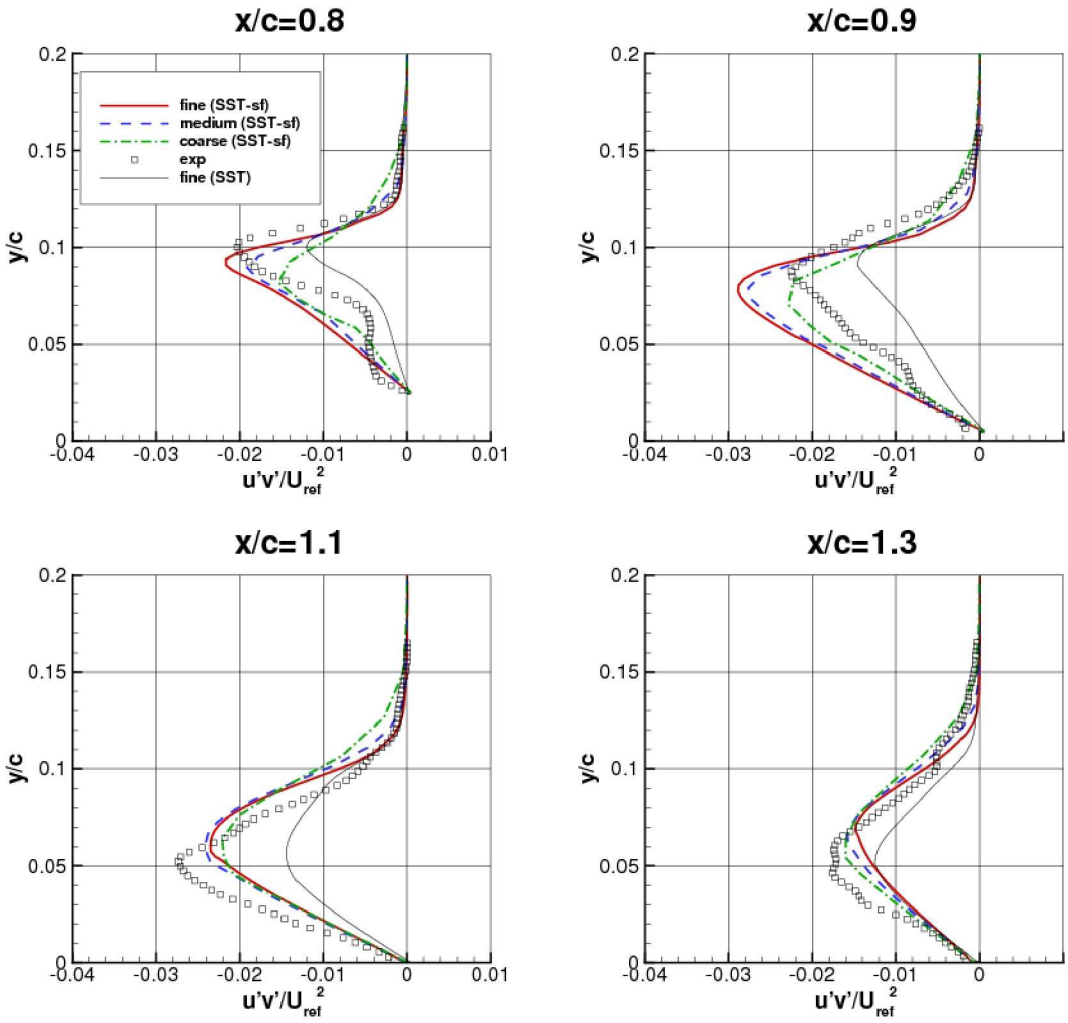

Figure 31. Profiles of turbulent shear stress at four stations on the 2-D hump grid, no flow control.

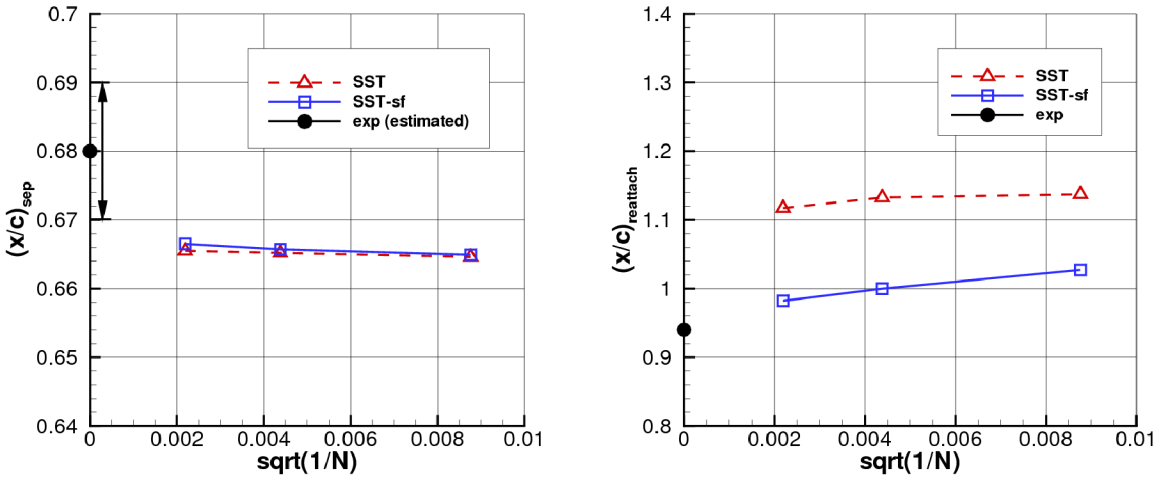

Figure 32. Separation and reattachment locations for the 2-D hump, steady suction flow control.

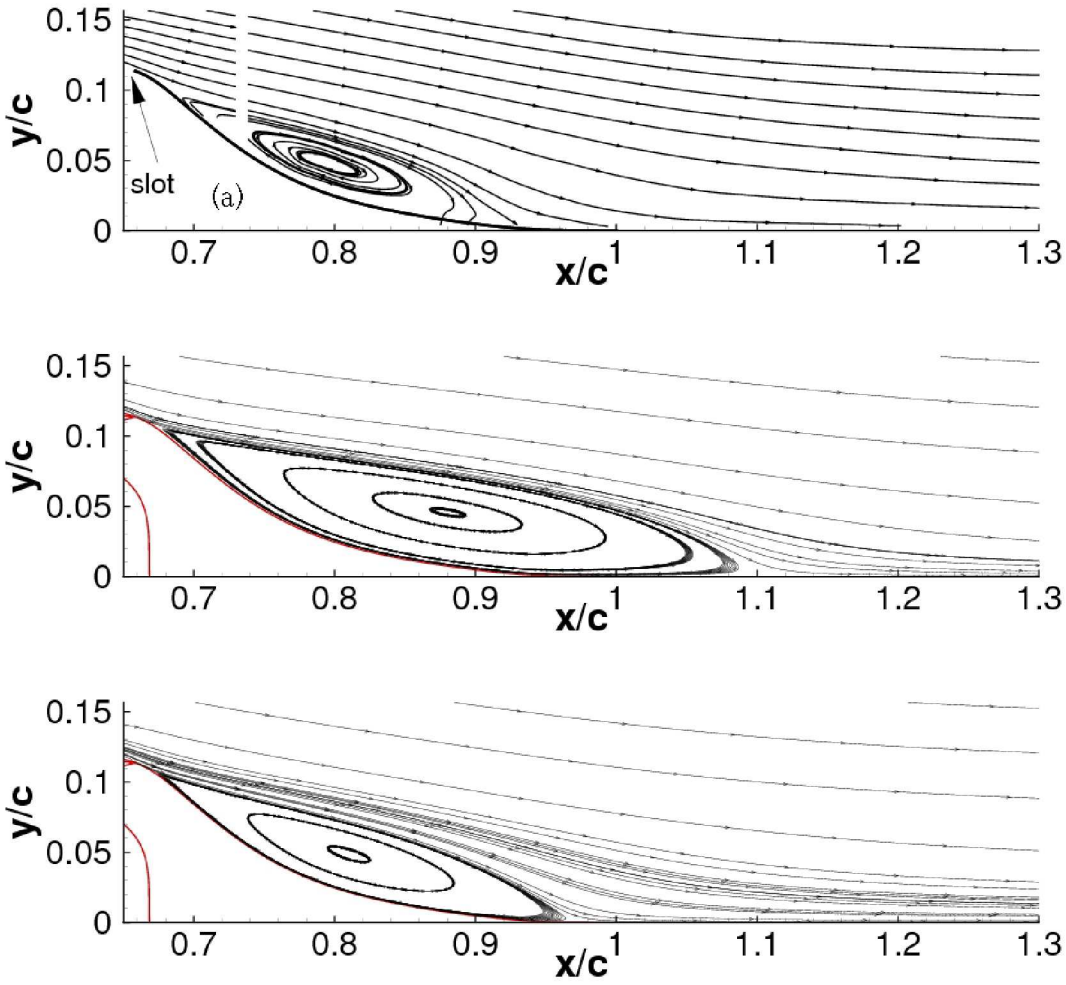

Figure 33. Streamlines for the 2-D hump, steady suction flow control (fine grid); (a) experiment, (b) SST, (c) SST-sf.

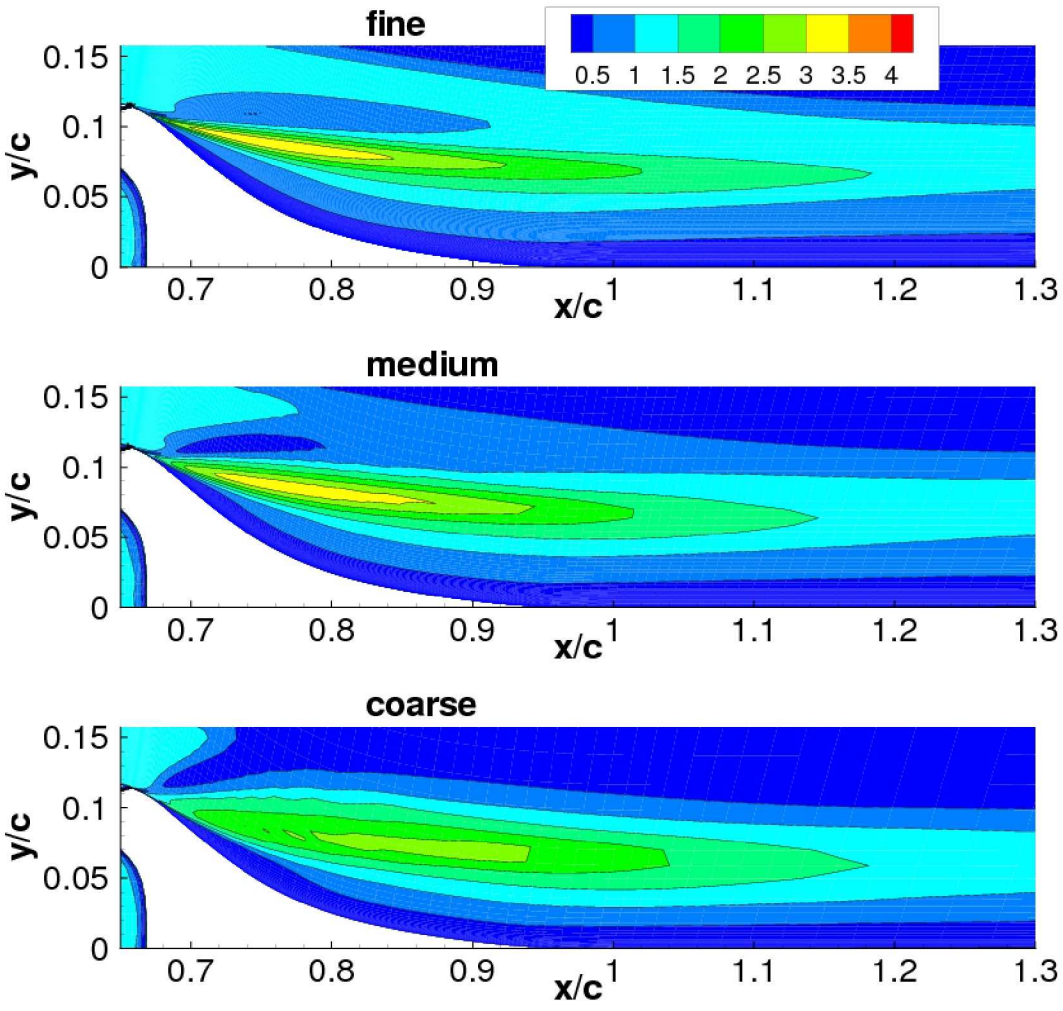

Figure 34. Contours of $\mathcal{P}/\varepsilon$ on three different grid sizes for the 2-D hump, steady suction flow control.

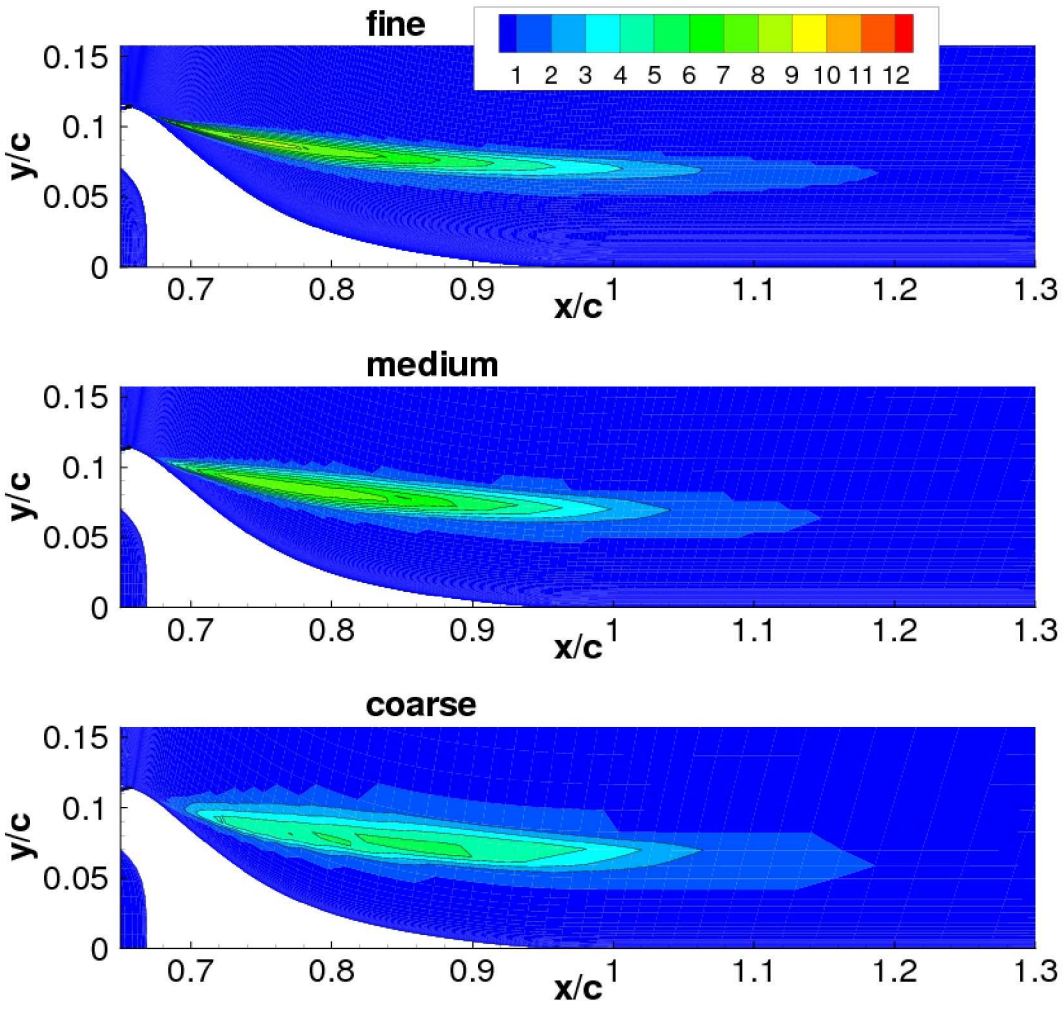

Figure 35. Contours of F_{sf} on three different grid sizes for the 2-D hump, steady suction flow control; SST-sf model.

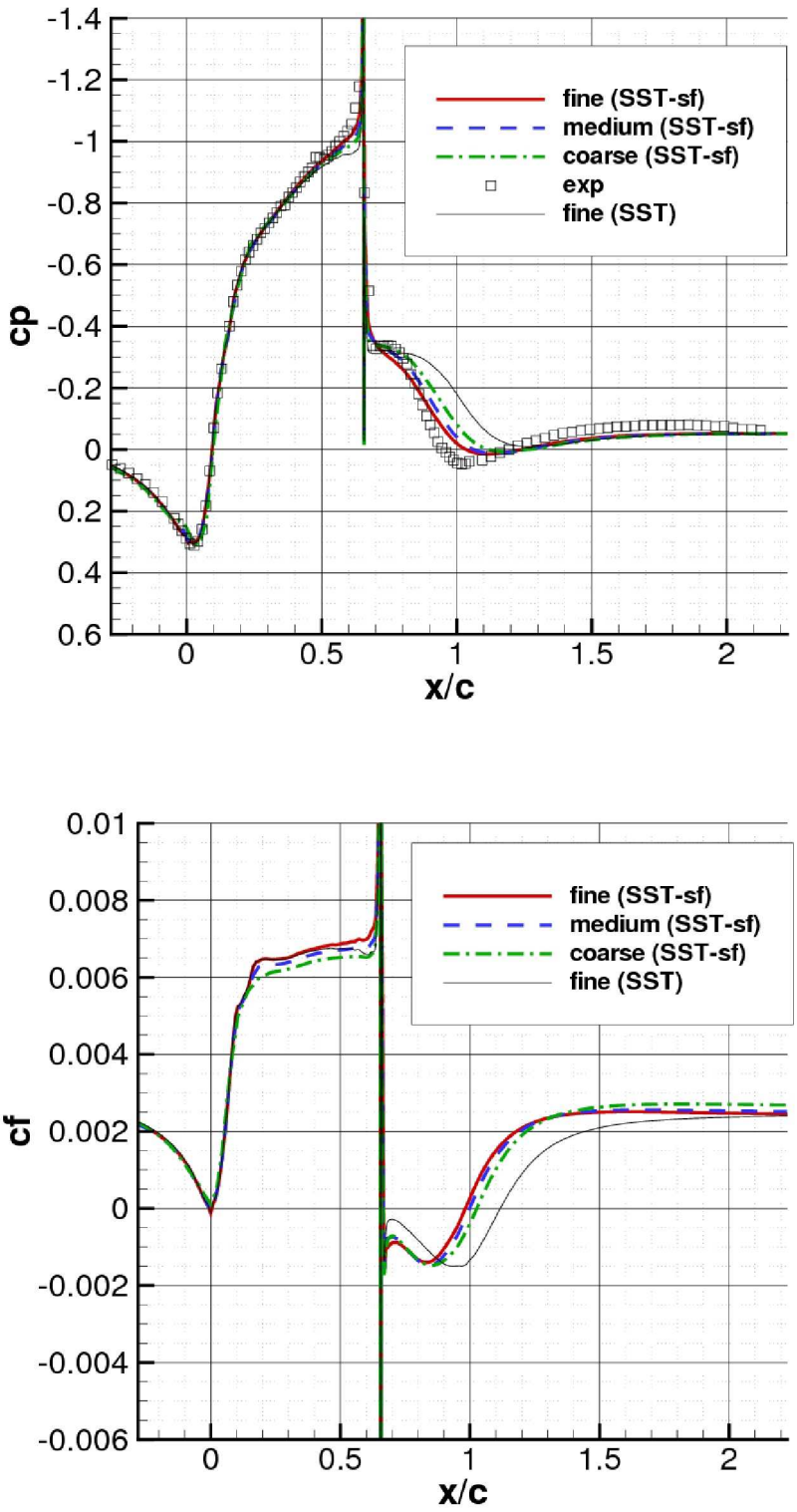

Figure 36. 2-D hump steady suction flow control results; (a) surface pressure coefficient, (b) surface skin friction coefficient.

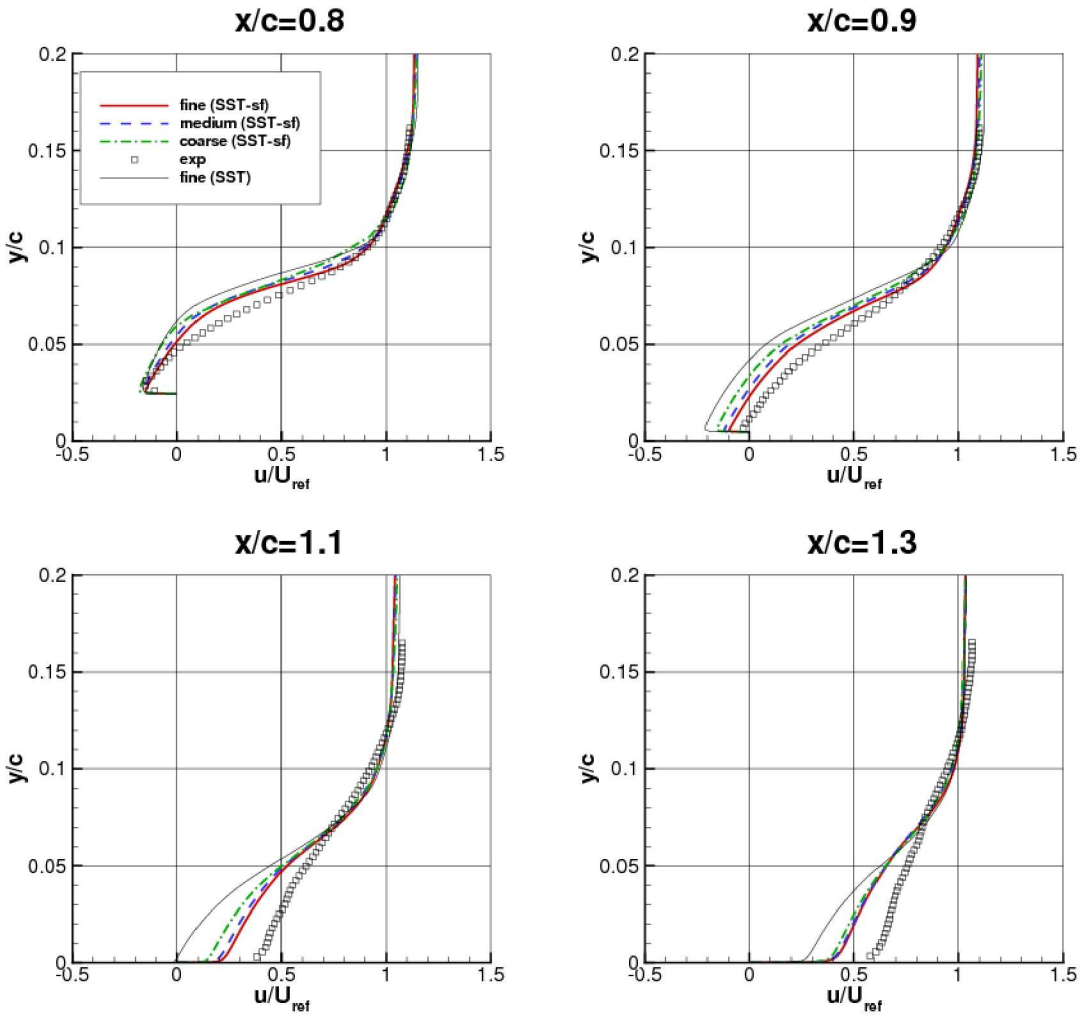

Figure 37. Profiles of horizontal velocity component at four stations on the 2-D hump grid, steady suction flow control.

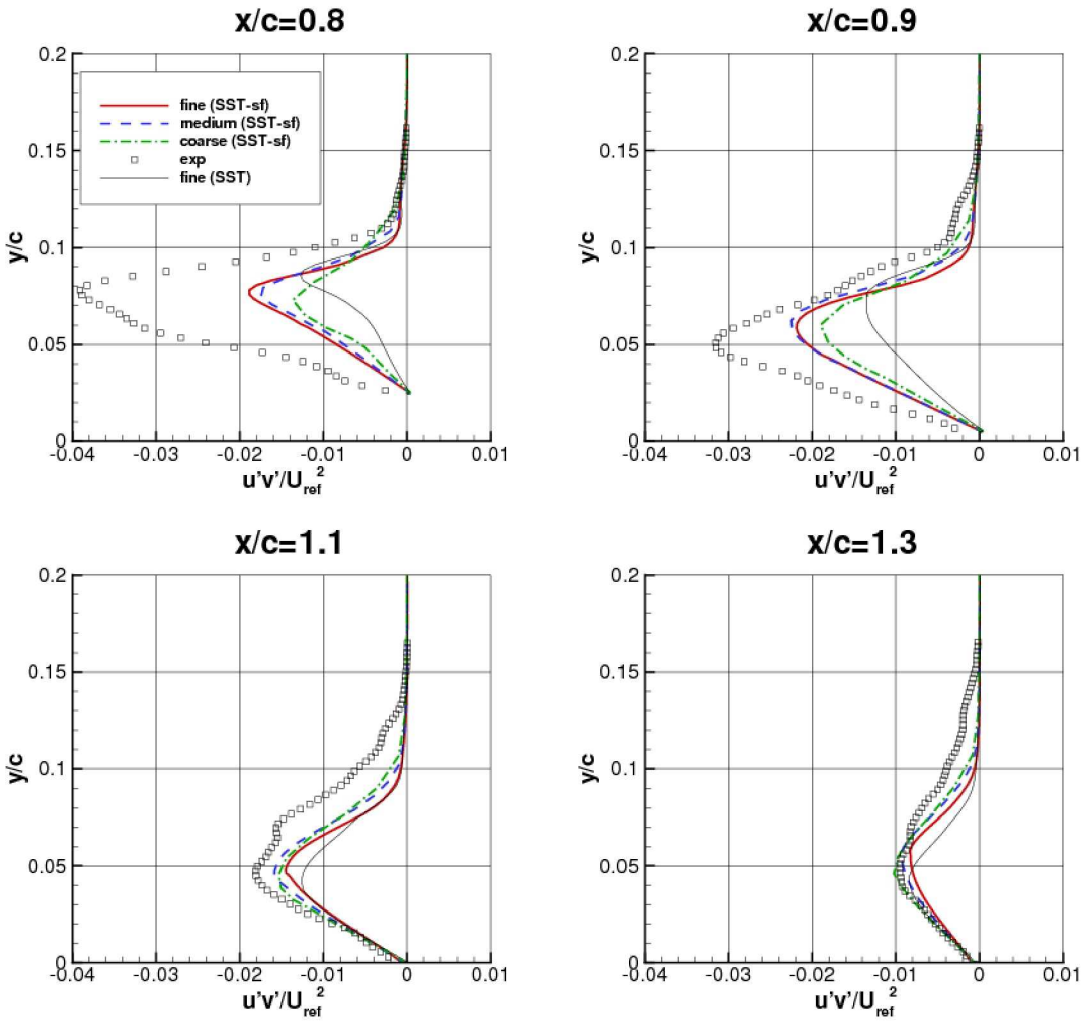

Figure 38. Profiles of turbulent shear stress at four stations on the 2-D hump grid, steady suction flow control.

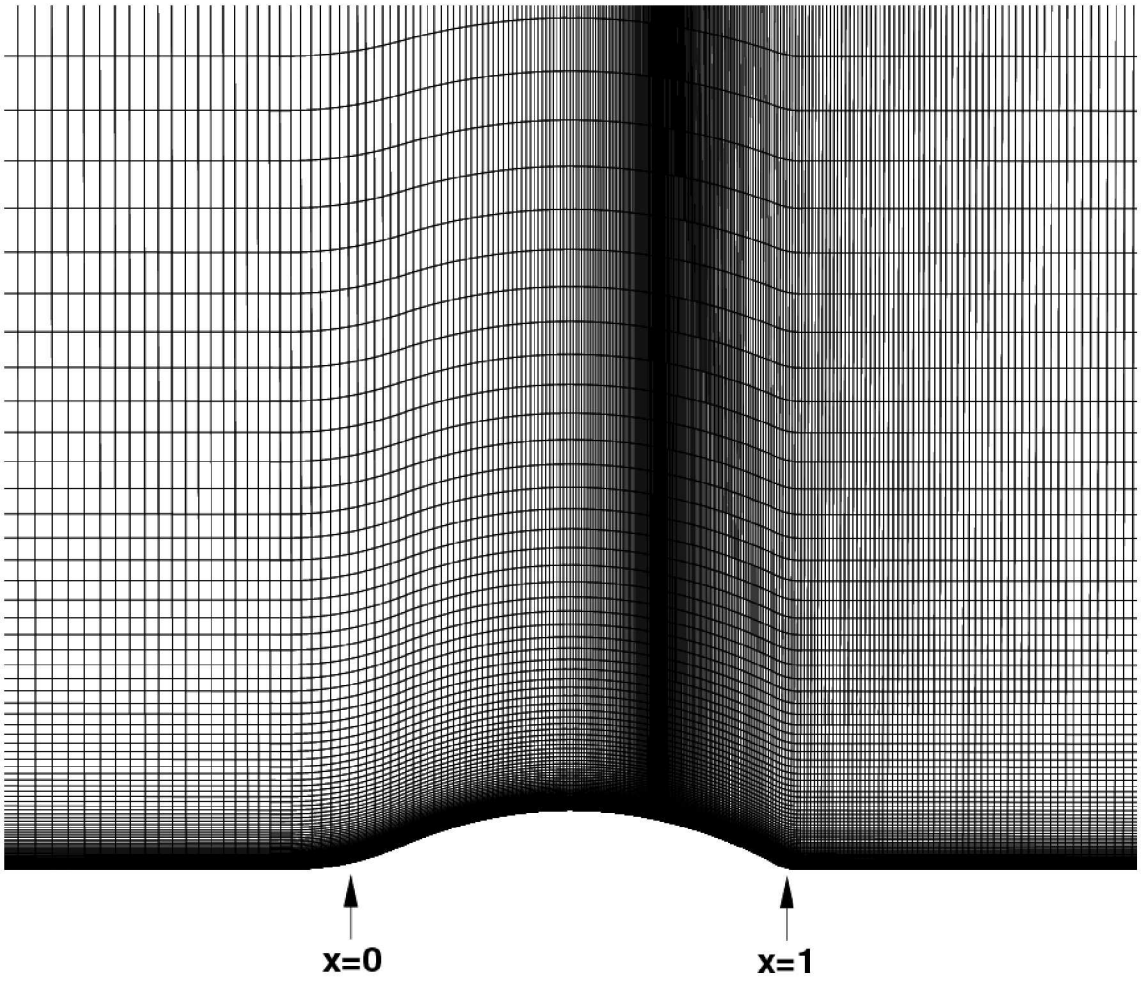

Figure 39. Portion of $2 \times 721 \times 321$ axisymmetric bump grid, with every other gridpoint shown.

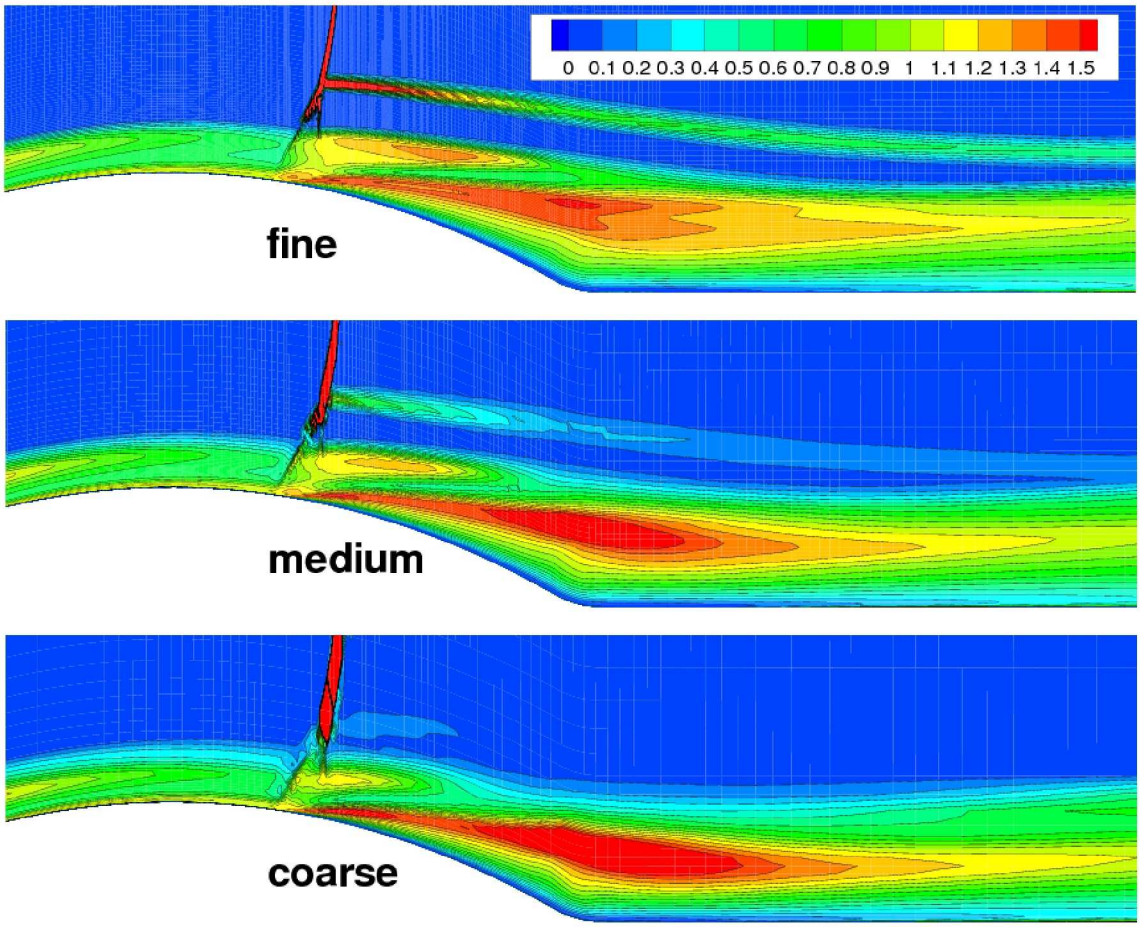

Figure 40. Contours of $\mathcal{P}/\varepsilon$ on three different grid sizes for the axisymmetric bump.

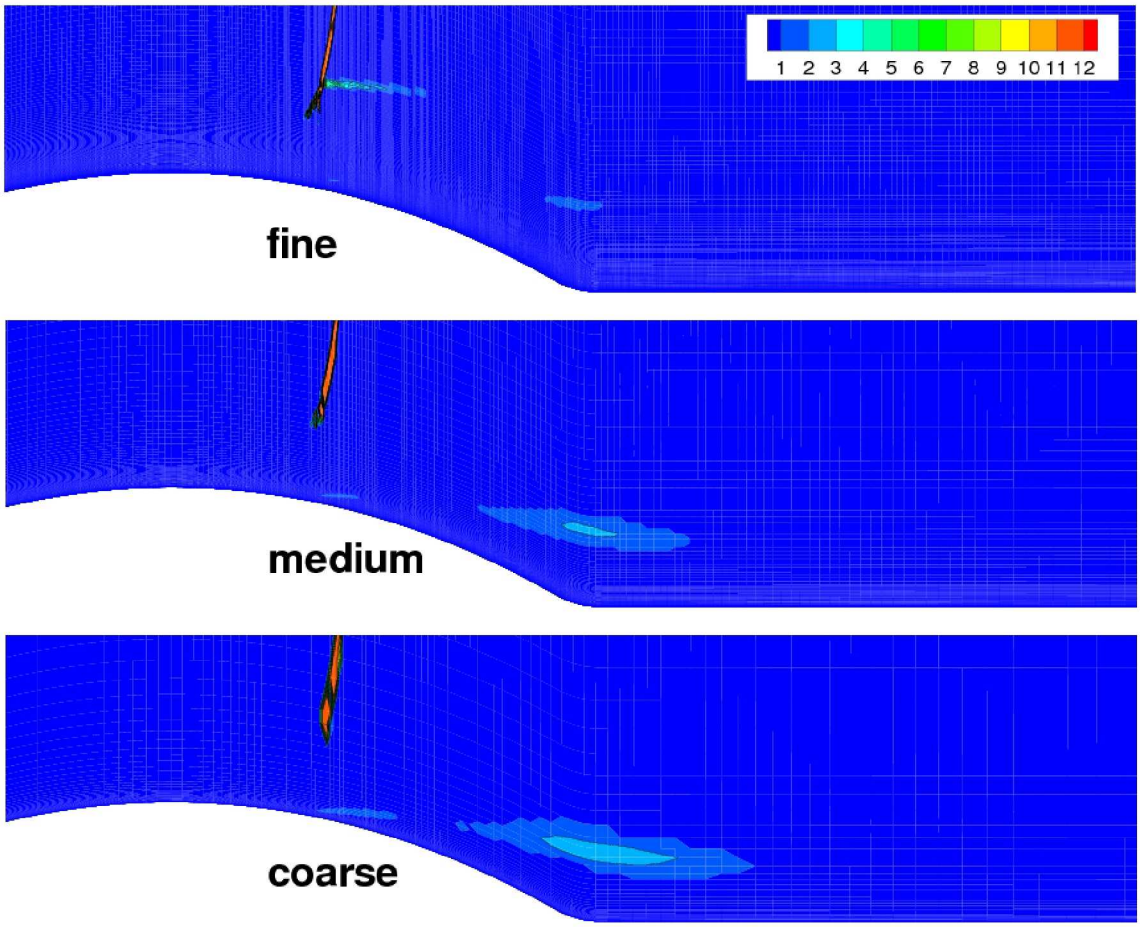

Figure 41. Contours of F_{sf} on three different grid sizes for the axisymmetric bump; SST-sf model.

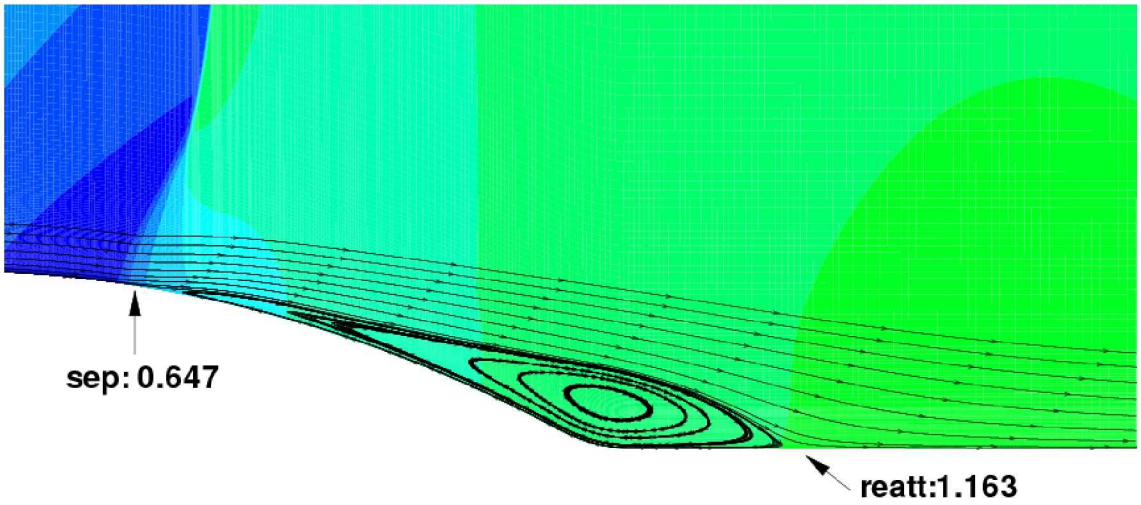

Figure 42. Streamlines for the axisymmetric bump (fine grid), colored by pressure contours to show the position of the shock; results are identical for both SST and SST-sf.

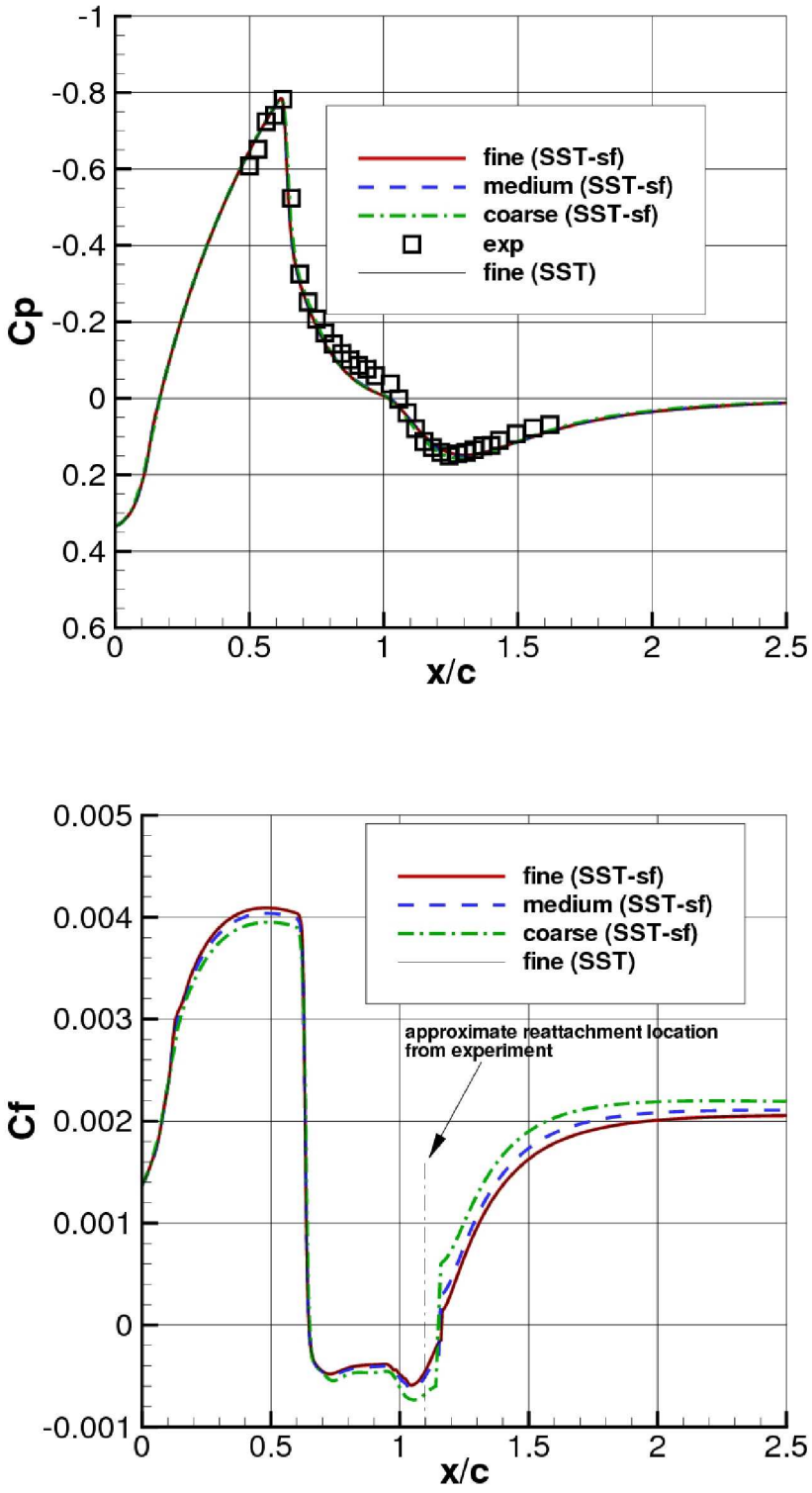

Figure 43. Axisymmetric bump results; (a) surface pressure coefficient, (b) surface skin friction coefficient.

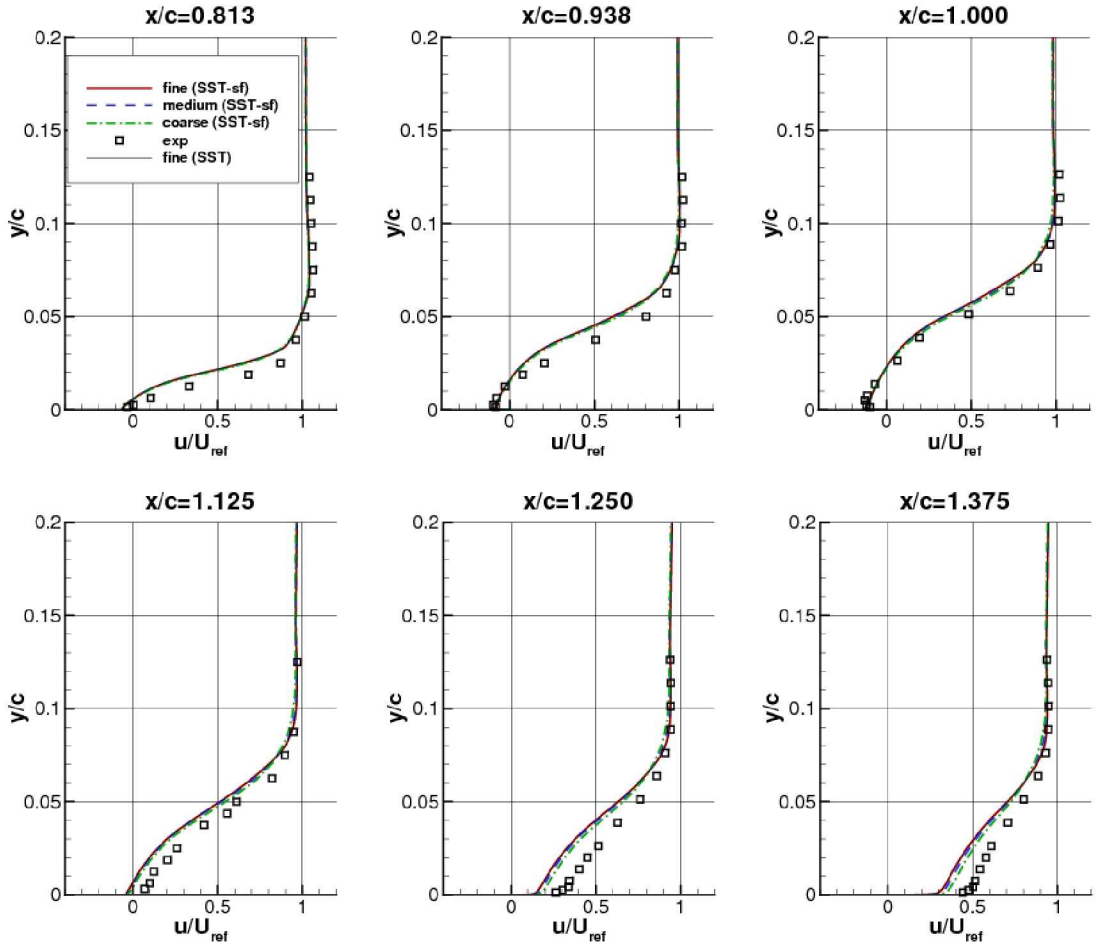

Figure 44. Profiles of horizontal velocity component at six stations on the axisymmetric bump.

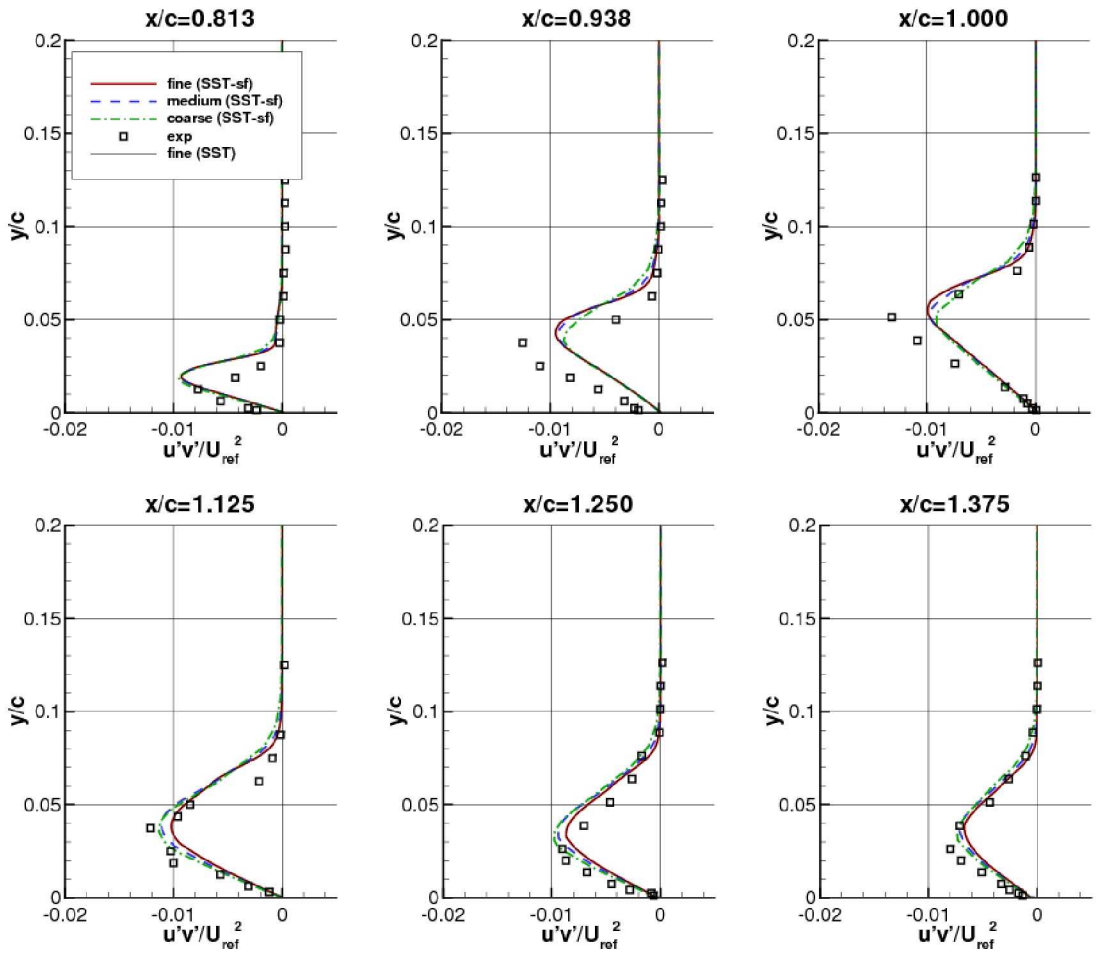

Figure 45. Profiles of turbulent shear stress at six stations on the axisymmetric bump.

REPORT DOCUMENTATION PAGE

Form Approved
OMB No. 0704–0188

1. REPORT DATE *(DD-MM-YYYY)*	2. REPORT TYPE	3. DATES COVERED *(From - To)*
01-12-2009	Technical Memorandum	

4. TITLE AND SUBTITLE
Exploring a Method for Improving Turbulent Separated-Flow Predictions with k-ω Models

5a. CONTRACT NUMBER

5b. GRANT NUMBER

5c. PROGRAM ELEMENT NUMBER

6. AUTHOR(S)
C. L. Rumsey

5d. PROJECT NUMBER

5e. TASK NUMBER

5f. WORK UNIT NUMBER
561581.02.08.07.20.15

7. PERFORMING ORGANIZATION NAME(S) AND ADDRESS(ES)
NASA Langley Research Center
Hampton, Virginia 23681-2199

8. PERFORMING ORGANIZATION REPORT NUMBER
L–19779

9. SPONSORING/MONITORING AGENCY NAME(S) AND ADDRESS(ES)
National Aeronautics and Space Administration
Washington, DC 20546-0001

10. SPONSOR/MONITOR'S ACRONYM(S)
NASA

11. SPONSOR/MONITOR'S REPORT NUMBER(S)
NASA/TM–2009–215952

12. DISTRIBUTION/AVAILABILITY STATEMENT
Unclassified-Unlimited
Subject Category 02
Availability: NASA CASI (443) 757-5802

13. SUPPLEMENTARY NOTES
An electronic version can be found at http://ntrs.nasa.gov.

14. ABSTRACT

A particular failing of Reynolds-averaged Navier-Stokes separated turbulent flow computations is addressed within the context of a k-ω two-equation turbulence model. The failing is the tendency for turbulence models to under-predict turbulent shear stress in the shear layers of some separation bubbles, yielding late boundary layer reattachment and recovery. Inspired by unpublished work of Volker, Langtry, and Menter, the author undertook an independent investigation in an attempt to improve the ability of the Menter shear stress transport (SST) model to predict flowfield characteristics in and downstream of separation bubbles. The fix is an ad hoc term that is a function of the local ratio of turbulent production to dissipation; it is used to multiply the ω-destruction term, increasing eddy viscosity in separated regions. With this fix, several flowfields are investigated. Results show that, although the "separation fix" can provide dramatic improvement in some cases, it is not consistently good for all flows. Thus, although it may prove helpful in many situations in its current form, this model may benefit from further refinements, including better sensitization to the energetics of turbulence in the separated region.

15. SUBJECT TERMS
CFD, turbulence model, separated flow, reattachment

16. SECURITY CLASSIFICATION OF:			17. LIMITATION OF ABSTRACT	18. NUMBER OF PAGES	19a. NAME OF RESPONSIBLE PERSON
a. REPORT	b. ABSTRACT	c. THIS PAGE			STI Help Desk (email: help@sti.nasa.gov)
U	U	U	UU	60	19b. TELEPHONE NUMBER *(Include area code)* (443) 757-5802